Impacts of sea level rise on hypoxia in the Chesapeake Bay: A model intercomparison

Chesapeake Bay Program Report
October 2019

Pierre St-Laurent[1], Marjorie A. M. Friedrichs[1], Ming Li[2] and Wenfei Ni[2]

[1]Virginia Institute of Marine Science, William & Mary
[2]University of Maryland Center for Environmental Science

Publication Date: October 2019

CBPO Publication Number: CBP/TRS-329-19

Suggested Citation:

St-Laurent, P., M.A.M. Friedrichs, M. Li and W. Ni, 2019. Impacts of sea level rise on hypoxia in the Chesapeake Bay: A model intercomparison. Report to the Chesapeake Bay Program, Annapolis, MD, 34 pp.

Cover graphic from: Chesapeake Bay Foundation

Executive summary

Over the recent years a number of studies have examined the effects of climate change and sea level rise (SLR) on hypoxia in Chesapeake Bay. However, variations in the methodology, the years considered, and the metrics reported made comparisons between these studies difficult. To clarify the effects of SLR on the Bay's hypoxia, we present an intercomparison between four numerical models following a common methodology. The models share the riverine fluxes, baseline period (1991–1995), and consider the same three scenarios of SLR: an increase in sea level of 0.17 m, 0.50 m, and 1.00 m (representative of years 2025, 2050 and 2100, respectively). SLR is the sole climate driver considered in these experiments.

There is considerable agreement between the models in how salinity changes in response to SLR. Salinity increases throughout the Bay and throughout the water column with little seasonality. The changes are amplified with increasing SLR but their spatial distributions remain similar. The models do not suggest an appreciable change with SLR in the top-to-bottom salinity contrast. The model projections for salinity are quantitatively close to those of earlier studies.

The models agree that SLR, in absence of other drivers of climate change, produces slightly warmer water temperatures in November–January and slightly cooler water temperatures in May–July. The changes are amplified with increasing SLR but their spatial distributions remain similar. The models exhibit some variations in the vertical structure of the changes in temperature (either concentrated in the upper 10 m or more vertically homogeneous). The magnitude of the changes in temperature due to SLR are substantially smaller than those associated with global warming.

The models agree that SLR decreases dissolved oxygen concentrations (DO) in the upper part of the water column and increases bottom DO at least in parts of the deep channel in May–July. Both negative and positive DO anomalies are amplified by SLR but the seasonal and spatial patterns remain similar. The vertical profiles of DO are uplifted by SLR and this feature accounts quantitatively for the negative DO anomaly of the upper part of the water column. The positive DO anomaly apparent in the bottom layer of the deep channel in the summer cannot be explained by changes in water solubility. Similarly, changes in the advection/diffusion of DO in response to SLR cannot account for the positive bottom DO anomaly. Instead, the models point toward a decrease in bottom-layer respiration as the cause of the positive bottom DO anomaly.

Focusing on the variables that affect bottom-layer respiration, we find that the slightly cooler water temperatures during summer, combined with the temperature-dependent respiration rates of the models, can account for the decrease in bottom layer respiration. Despite the similarities between the model results, the magnitude and duration of the positive bottom DO anomaly show substantial variations from one model to another. Further examination of the model parameterizations suggest that differences in the temperature sensitivity and the primary production are likely responsible for differences in the magnitude/duration of the positive bottom DO anomaly.

The hypoxic volume, a metric commonly used in studies of hypoxia, was found to be poor indicator of changes in DO concentrations within the deep channel of the Bay (where hypoxia and anoxia are most prevalent). The boundary of the hypoxic zone (isosurface of DO=2 mg L^{-1}) often lies close to (or lies inside) shallow areas where the models project DO to decrease in response to SLR. In these cases, the hypoxic volume will expand with SLR, regardless of the presence/absence of a positive DO anomaly within the deep channel. The result emphasizes that consistent metrics should be used when comparing model studies of hypoxia.

1 Introduction

Dissolved oxygen (DO) concentrations have been an important issue for the Chesapeake Bay since at least the 1950's (*Hagy et al.*, 2004). The negative impacts on fish habitat and the harvest of species such as blue crabs have motivated a number of modeling studies focused on examining future changes in the Bay's DO in response to climate drivers. Although these studies agree that warming temperatures will exacerbate Chesapeake Bay hypoxia, they have shown mixed responses to sea level rise (SLR), *i.e.*, both improvements and degradation of DO concentrations.

In an experiment focused on the period 1993–1995 and using the model ChesROMS-ECB, *Irby et al.* (2018) reported improvements in bottom DO in the mesohaline region[1] of the Bay and degradations in the oligohaline and polyhaline regions in response to a +0.50 m increase in sea level (see their Table 3). The cumulative hypoxic volume, defined as the annually-integrated volume of water with DO < 2 mg L^{-1}, decreased by 12 km^3 days in the same experiment (*i.e.*, an overall improvement for the Bay; their Table 4).

Wang et al. (2017) simulated the effect of a +0.50 m increase in sea level relative to the period 1991–2000 using the Chesapeake Bay Program's Water Quality Sediment Transport Model (WQSTM). The summer anoxic volume was found to decrease by 14.4% in response to the perturbation, which is qualitatively consistent with the results of *Irby et al.* (2018). On the other hand, a third model (UMCES-ROMS-RCA) suggested a +0.5 km^3 increase in the hypoxic volume and a +0.1 km^3 increase in the anoxic volume in the month of August in response to sea level rise of +0.50 m (*Ni et al.*, 2017).

Variations in the methodology, period of time investigated, and metric reported (*e.g.*, DO concentrations, hypoxic/anoxic volume) make comparisons between these results particularly challenging. The goal of the present study is to offer some clarifications by presenting a model intercomparison where SLR is the sole climate driver considered and the methodology is uniformized as much as possible (see Methods).

The report is divided into four sections. The first two sections explore the changes in the physical fields (salinity S and temperature T) in response to SLR (§3.1,§3.2). These two fields determine the solubility of oxygen in seawater independently of biogeochemical processes. Section 3.3 illustrates the changes in DO concentrations projected by the models included in this intercomparison. Finally, the mechanisms responsible for these changes in DO concentrations are discussed in §4.

2 Methods

2.1 Model experiments

This study includes one reference simulation and three scenarios where the sea level is increased relative to the reference simulation. The reference simulation covers the period Jan. 1991 to Dec. 1995. This five year period is commonly used for management purposes by the Chesapeake Bay Program as it includes both "wet" and "dry" years corresponding to high/low riverine freshwater discharge (respectively). The models use realistic oceanic and atmospheric forcings during this period and they share the same hydrologic forcing. This hydrologic forcing is the Phase-6 results of the Chesapeake Bay Program Watershed Model (*Shenk and Linker*, 2013) and features watershed fluxes for freshwater and biogeochemical variables at daily frequency.

[1]The oligohaline, mesohaline and polyhaline regions are defined as those with average sea surface salinity < 5 psu, 5 to 15 psu, and > 15 psu, respectively.

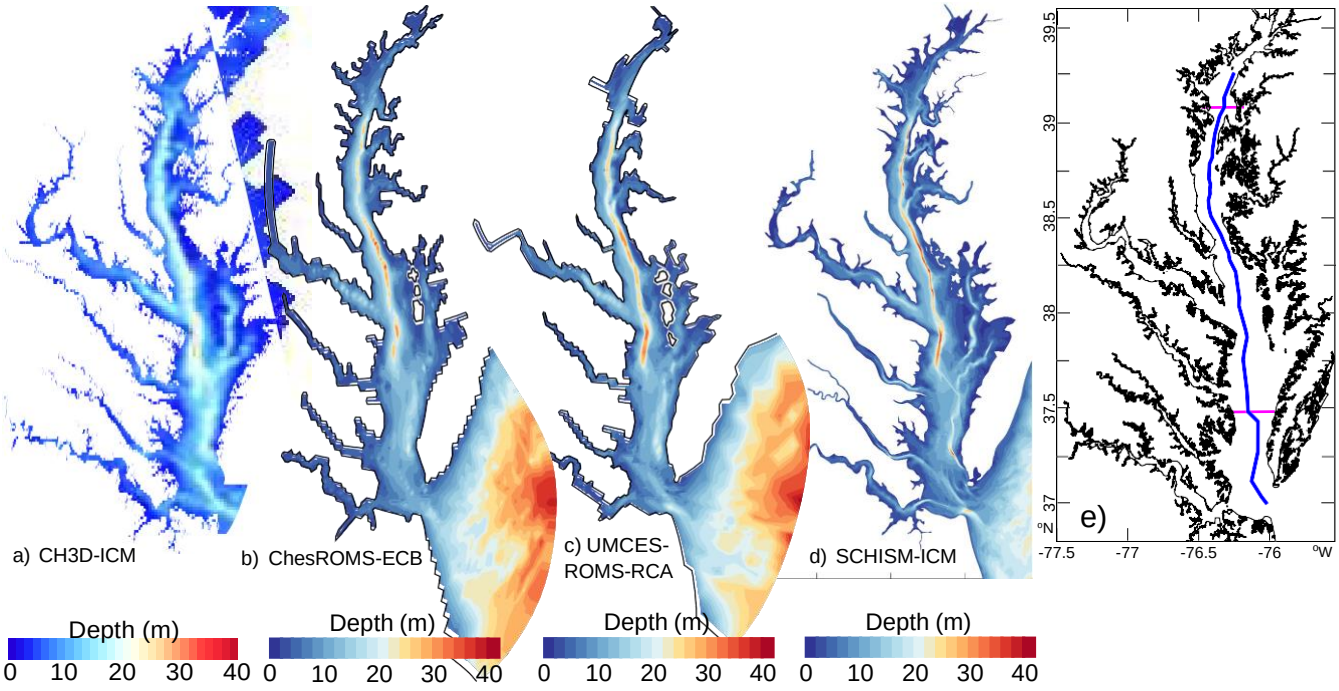

Figure 1: Bathymetry and geographical extent of the four numerical models used in the study. (a) CH3D-ICM, (b) ChesROMS-ECB, (c) UMCES-ROMS-RCA, and (d) SCHISM-ICM. In the case of SCHISM-ICM, the model domain reaches beyond the shelf break (see *Ye et al.*, 2018) and thus only a fraction is shown here. (e) South-North transect used in the study (blue, similar to that of *Cerco et al.* (2013)). A shorter transect (bounded by the magenta lines) is used in certain figures.

The three SLR scenarios correspond to an increase in sea level (ΔSL) of +0.17 m, +0.50 m, and +1.00 m relative to the reference period (1991–1995). These values are assumed to be roughly representative of the period surrounding years 2025, 2050, and 2100 (respectively). We note that the fact that the position of the surface differs between these experiments complicates the comparison of vertically-varying fields (such as DO). In this report, the vertical axis of the figures is defined in relation to the geoid, a time-invariant equipotential surface represented by $z = 0$ (z is positive upward). The reference $z = 0$ matches approximately the mean sea surface height of the reference simulations. In the three experiments that include SLR, the mean sea surface is approximately at $z \approx +0.17$ m, $z \approx +0.50$ m or $z \approx +1.00$ m (respectively; see Table 1).

Another complication of the SLR experiments relates to the prescription of oceanic properties along the models' open boundary (see Figure 1 for their location). As the sea level rises, an assumption must be made on how these oceanic properties at the open boundary are modified. In this study, we assume that a property $\phi(z)$, prescribed at a given time and point of the boundary in the reference simulation, will be shifted upward by SLR by a distance:

$$\Delta \mathrm{SL} \left(1 + \frac{z}{H}\right), \tag{1}$$

where H is the local mean water depth in the reference simulation ($H > 0$) and $z = -H$ at the sea floor (*e.g.*, *Shchepetkin and McWilliams*, 2005, their Equation 1.9). The upward displacement is thus proportional to ΔSL and proportional to the distance from the bottom (zero at the bottom). No modifications to the oceanic properties of the open boundary are made other than this vertical "stretching". The same assumption is used in the different models irrespective of their vertical coordinate system.

The sea level perturbation (ΔSL) is added to the sea surface height of the reference period (1991–1995) during a "spin-up" period when the model variables adjust themselves to the modification. After this period of spin-up, the models simulate the period 1991–1995 exactly as in the reference simulation except for the modification in sea level. This study is primarily concerned with comparing the five year-averaged state obtained by the four models in those four simulations. The transient adjustments taking place during the spin-up period, or the year-to-year variations during the period 1991–1995, are not the focus of this study.

Table 1: Model experiments conducted in the study. The experiments are identical to the reference simulation except for the change in sea level (SL). Experiments for which model results are available are indicated by the X symbol. All four model experiments have a duration of 1826 days (5 years).

Model experiment	CH3D-ICM	ChesROMS-ECB	UMCES-ROMS-RCA	SCHISM-ICM
1. Reference run (1991–1995)	X	X	X	X
2. ΔSL = +0.17 m (ca. 2025)	X	X	X	X
3. ΔSL = +0.50 m (ca. 2050)	X	X	X	X
4. ΔSL = +1.00 m (ca. 2100)		X	X	X

The four models considered in this intercomparison are WQSTM (*Wang et al.*, 2017), ChesROMS-ECB (*Da et al.*, 2018), UMCES-ROMS-RCA (*Testa et al.*, 2014), and SCHISM-ICM (*Ye et al.*, 2018). WQSTM is composed of a physical model (CH3D) and a water quality model (ICM) and will be referred to as CH3D-ICM throughout this report. CH3D, ChesROMS-ECB and UMCES-ROMS all use structured grids with horizontal resolutions substantially coarser (1–2 km in the main stem of the Bay) than SCHISM-ICM (~ 280 m) which affects the representation of bathymetric features (Figure 1). SCHISM-ICM is the

only model in the intercomparison featuring an unstructured grid, explicit representation of inundation, and a model domain extending farther offshore than the other models, reaching beyond the shelf break of the Mid-Atlantic Bight. All the models compute the physics and biogeochemistry separately (using physical fields saved at a tide-resolving interval) except for ChesROMS-ECB which solves physics and biogeochemistry simultaneously.

Results from ChesROMS-ECB and UMCES-ROMS-RCA are directly available for the analyses of this study. For the other two models, the participants created the figures necessary for the intercomparison and provided them to the first author. Note that no model results are available from CH3D-ICM for the case +1.00m (Table 1).

2.2 Intercomparison of the model experiments

Hypoxia is most prevalent in the bottom layer of the deep channel oriented south-north along the Bay (Figure 1). This channel is illustrated in south-north transects to simultaneously represent vertical and longitudinal variations within the Bay. The transect covers the majority of the Bay down to its mouth (Figure 1e) except in specific cases where only the deep channel is represented. When illustrating changes in response to SLR, the changes are computed at a same z (or, equivalently, at a same distance from the seabed). For example, given a variable such as salinity that increases with depth, an upward translation of the halocline (caused by SLR) would appear as a large positive anomaly at the original position of the halocline. Note also that the figures illustrating changes in response to SLR are all bounded vertically by $z = 0$ m since there is no information available from the reference simulation above this point.

The model outputs are averaged in time to create a monthly climatology for the five years of the simulations. The analyses mostly focus on the summer months (hypoxia generally peaks in July) but also extend into the winter months for temperature. The variables selected for the intercomparison are salinity (S), temperature (T), and dissolved oxygen (DO). The changes in response to SLR are denoted as ΔS, ΔT, ΔDO and are computed by subtracting the value of the reference run from the values of experiments 2–4 (Table 1). S and T are important variables as they define the maximum concentration of oxygen in seawater ($DO_{sat}(T, S)$). The change in DO_{sat} due to ΔT and ΔS is computed as:

$$\Delta DO_{sat} = DO_{sat}(T + \Delta T, S + \Delta S) - DO_{sat}(T, S), \quad (2)$$

which can be compared to ΔDO to infer the relative importance of solubility effects and biological effects.

CH3D-ICM differs from the three other models by having its oceanic boundary positioned at the Bay's mouth (Figure 1). In this configuration, the properties simulated at the Bay's mouth are substantially influenced by the conditions prescribed at the open boundary. Previous experiments with CH3D-ICM resulted in SLR causing changes in salinity within the Bay that were substantially lower (*Brady et al.*, 2018) than those reported by *Hong and Shen* (2012). To circumvent this limitation of the model, in this study the salinity prescribed at the oceanic boundary of CH3D-ICM is increased throughout the water column by $0.4(\Delta SL)/0.5$. This increase in the salinity at the open boundary is in addition to the stretching of Equation 1. Note that salinity is the only field of CH3D-ICM for which such an adjustment is made at the open boundary.

3 Results

3.1 Changes in salinity

Salinity increases in response to SLR throughout the Bay and throughout the water column (Figures 2,3,4). ΔS is largest in the upper 10 m, *i.e.* where the vertical salinity gradient is strongest and indicates an upward translation of the halocline with SLR (see §2.2). The salinity profiles in the cases that include SLR follow approximately:

$$S(z') + constant, \qquad z' = z + \Delta \mathrm{SL}\left(1 + \frac{z}{H}\right), \tag{3}$$

where $S(z)$ is the profile of the reference run, z' represents the stretching of Equation 1, and *constant* is a bay-wide spatial average of the increase in salinity in a given SLR scenario. Note that the stretching does not substantially modify the salinity difference between the bottom and the surface. For example, in the reference simulation the average top-to-bottom salinity difference in the main stem is 5.83 psu in ChesROMS-ECB and 5.84 psu in UMCES-ROMS-RCA. The corresponding values in the case +1.00 m are 5.67 psu and 5.79 psu (*i.e.*, fairly similar to the reference simulation in both models). Overall, these results indicate that SLR produces minor changes in the top-to-bottom haline stratification.

The changes in S illustrated in Figures 2–4 are larger as SL increases, but the spatial distributions of ΔS remain the same for all SLR experiments. The Bay-averaged change in S is on the order of ~0.2–0.3 psu, ~ 0.7 psu and ~ 1.5 psu for a SLR of +0.17 m, +0.50 m and +1.00 m (respectively). No seasonality is apparent in ΔS.

Bay-wide maps of the change in July bottom salinity due to SLR confirm that the change in salinity affects the whole Bay (Figure 5,6,7). ΔS is larger in areas of bottom depth ≤ 10 m and lower in the deep channel, as expected from the transects of ΔS . On the continental shelf, the change in bottom salinity is typically small (≤ 0.2 psu) and appears white on the colorscale.

The models exhibit considerable agreement in their projections of changes in salinity with SLR. One exception is that CH3D-ICM shows its largest ΔS at the Bay's mouth (which coincides with the model's oceanic open boundary; see §2.2) while this is where the other models show the smallest changes in bottom S (Figures 5–6). In addition, CH3D-ICM shows negative bottom ΔS in the oligohaline Bay and in certain tributaries while the other models do not (Figures 5–6). In the main stem of the Bay, the ΔS of CH3D-ICM is better aligned with the other models but smaller in magnitude. For example, the Bay-averaged change in salinity for the case +0.50 m is ~ 0.5 psu in CH3D-ICM but closer to ~ 0.7 psu in the other three models (Figures 2–3). Overall, the model projections for ChesROMS-ECB, UMCES-ROMS-RCA and SCHISM-ICM are very close to those of *Hong and Shen* (2012) in terms of magnitude, spatial structure, and weak seasonality.

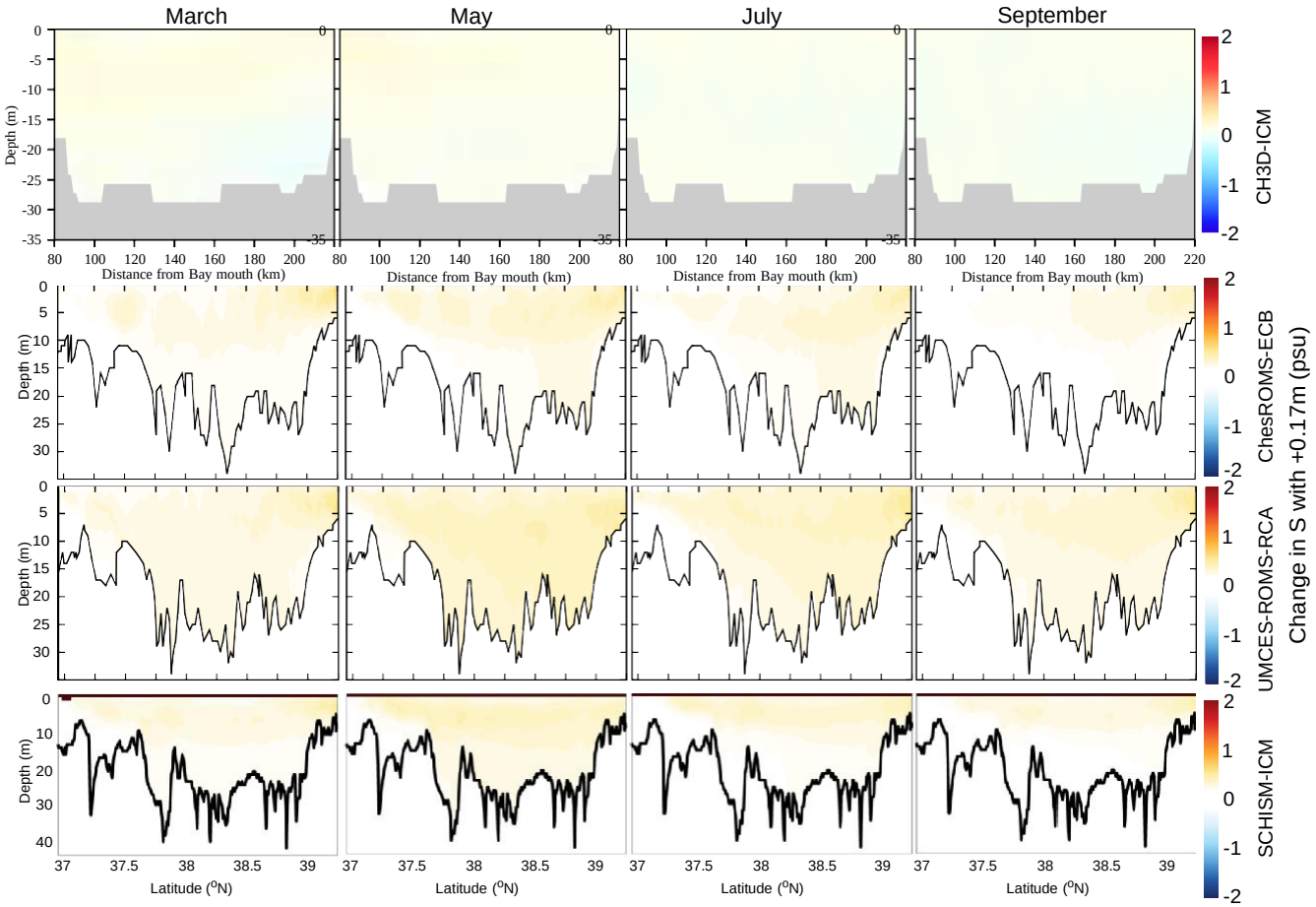

Figure 2: Change in salinity in response to a sea level rise of +0.17 m (ΔS). The rows represent the four models included in the intercomparison. The columns are months of the year (March, May, July, September). The figures correspond to the south-north transect depicted in Figure 1e (the transect is limited to the deep channel in CH3D-ICM).

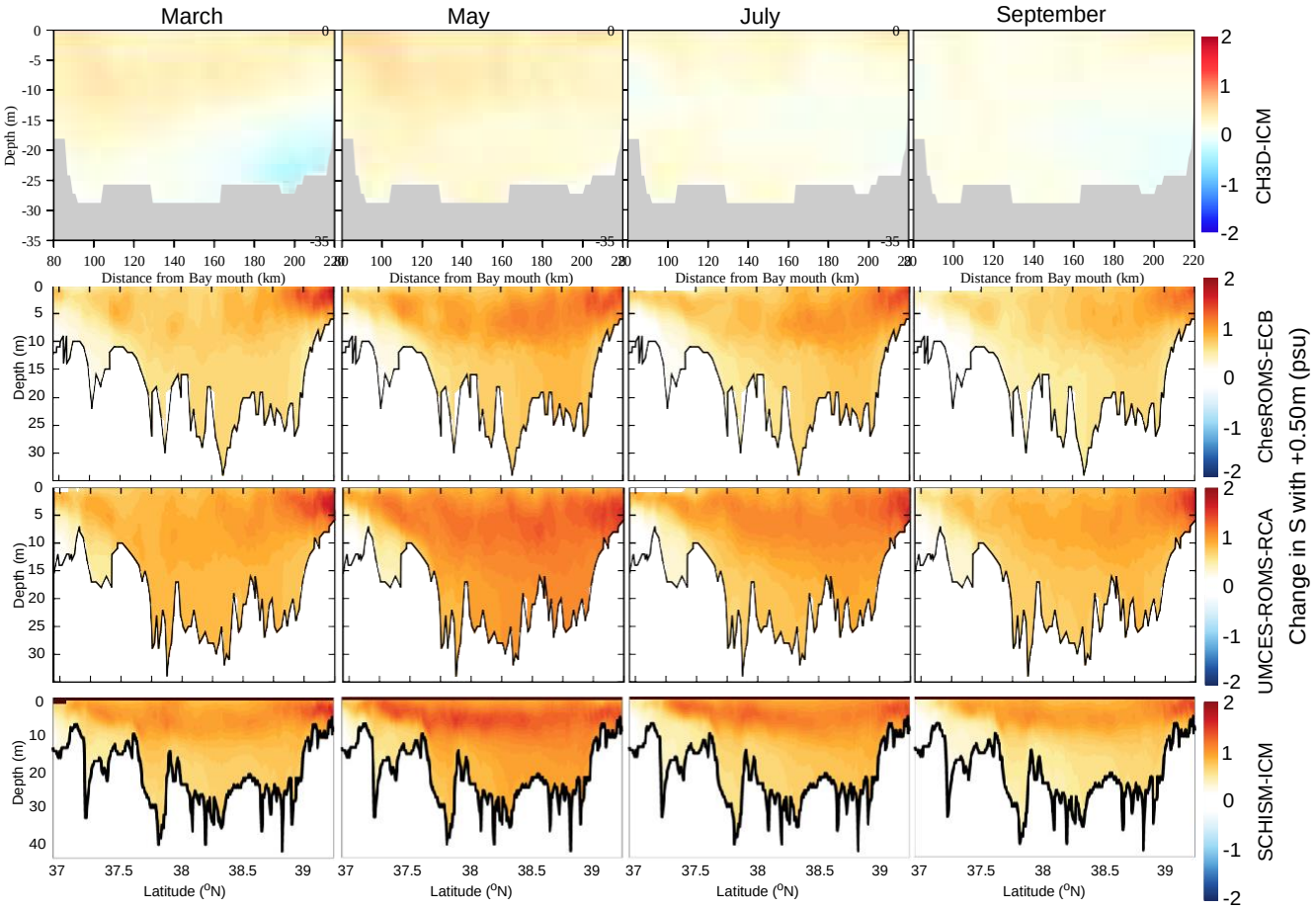

Figure 3: Same as Figure 2 but for a sea level rise of +0.50 m.

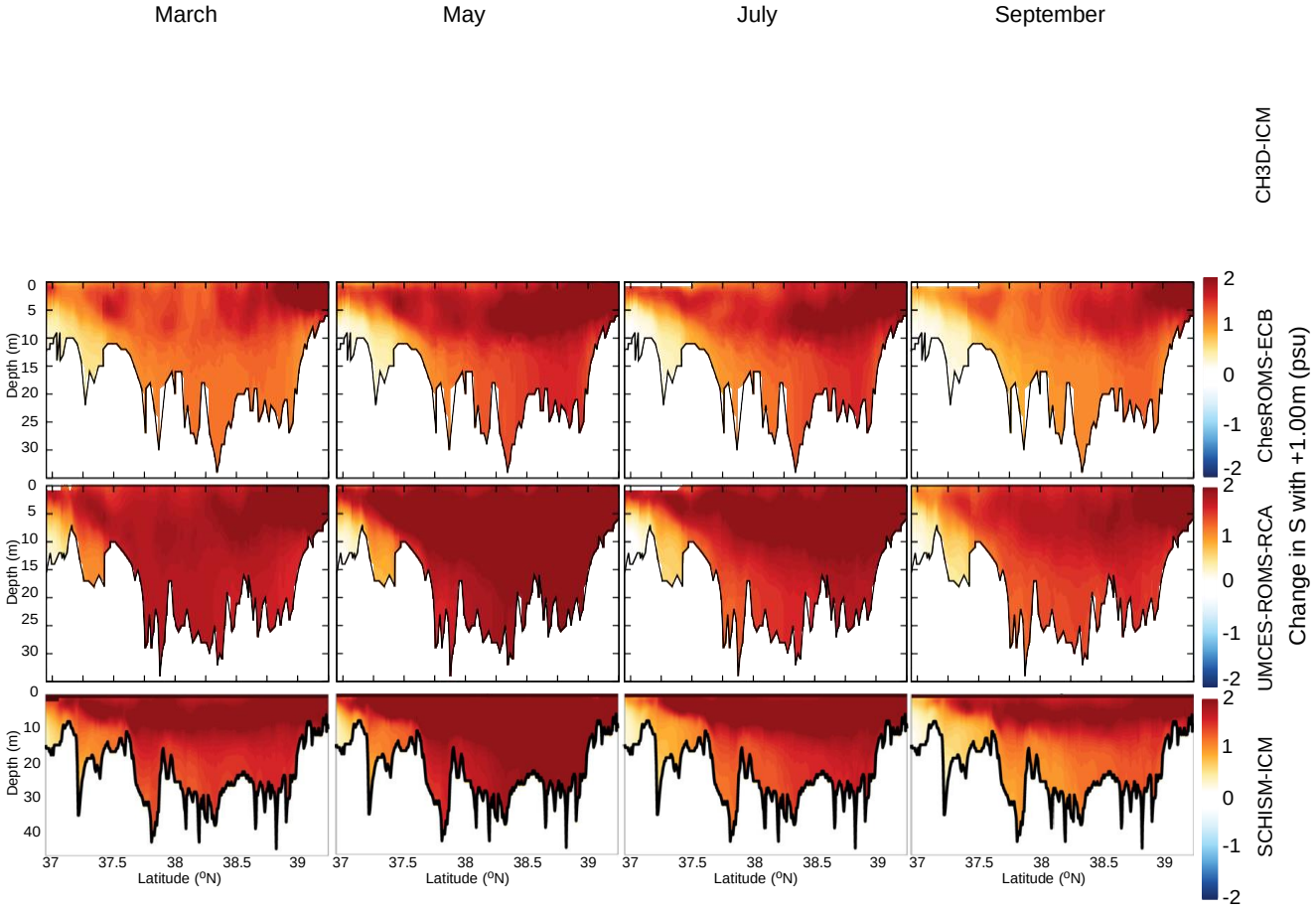

Figure 4: Same as Figure 2 but for a sea level rise of +1.00 m.

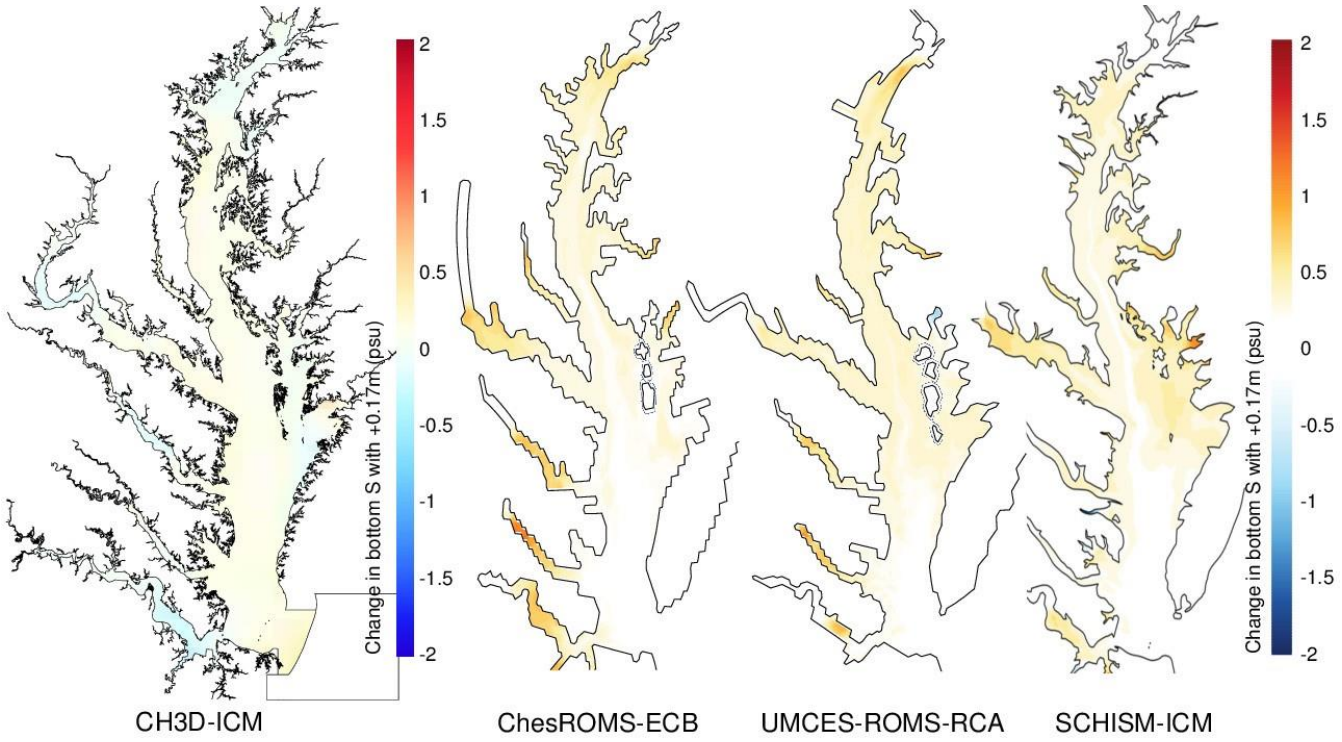

Figure 5: Change in bottom salinity in July in response to a sea level rise of +0.17 m.

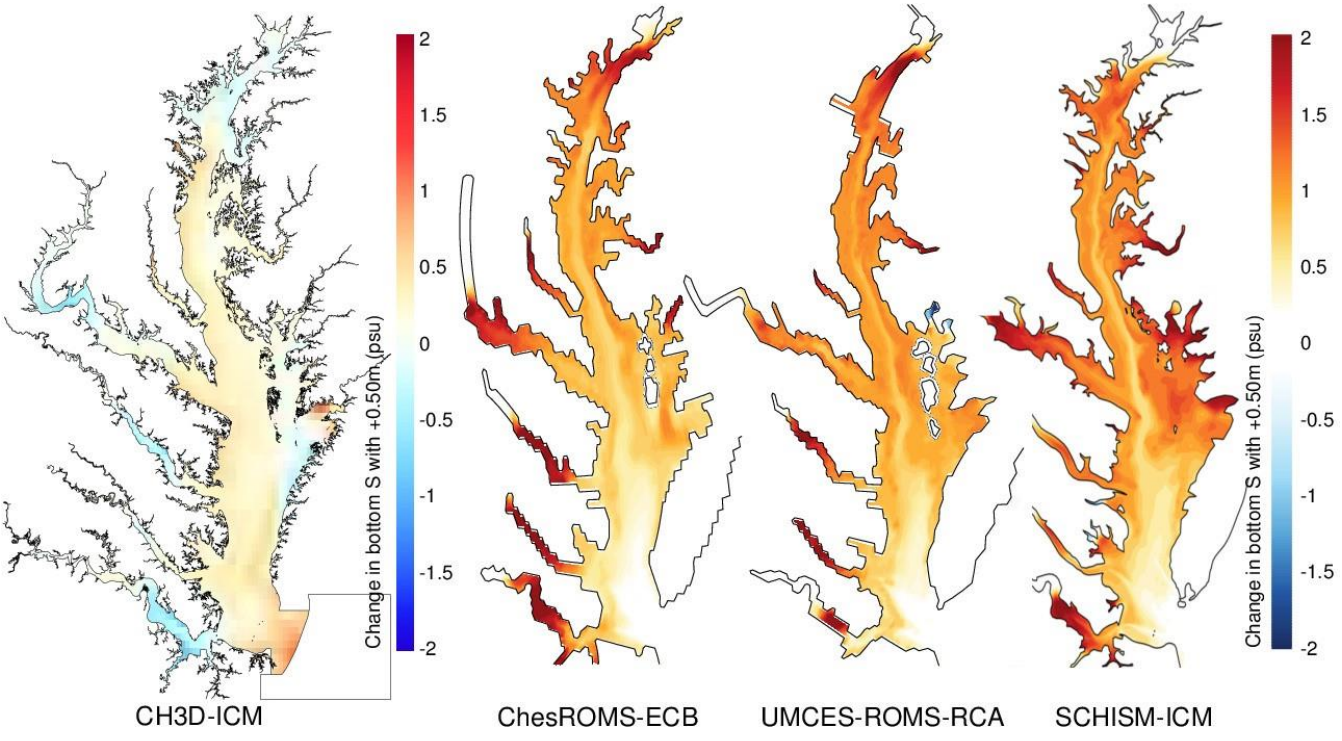

Figure 6: Same as Figure 5 but for a sea level rise of +0.50 m.

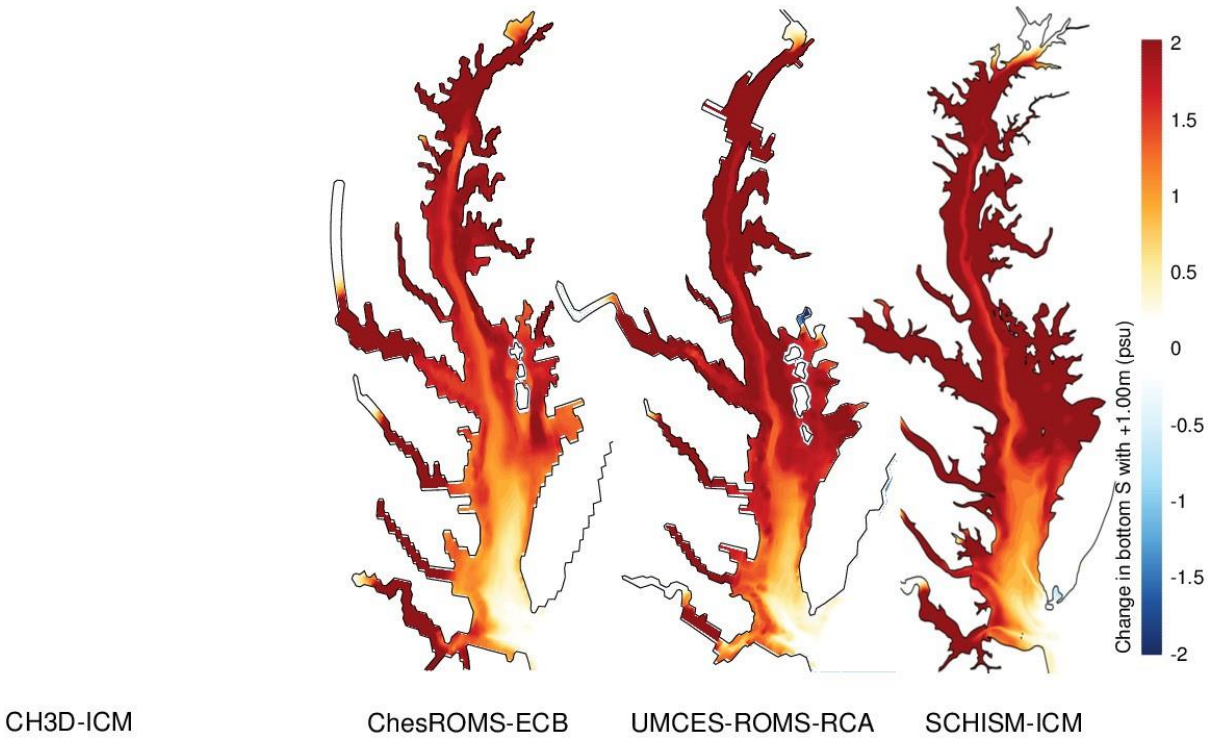

Figure 7: Same as Figure 5 but for a sea level rise of +1.00 m.

3.2 Changes in water temperature

All four models consistently show that water temperature both increases and decreases in response to SLR depending on the season (Figures 8–10). A positive ΔT is apparent during November–January and a negative ΔT is apparent in May–July. During January–May and during July-November (not shown in the figures), the models' ΔT transitions from one sign to another and exhibit either a mixture (positive and negative) or no change ($\Delta T \sim 0$). In the case +1.00 m, the temperature anomalies are clearly visible throughout the water column in all the models, but inter-model variations in the vertical structure of the anomalies are apparent. CH3D-ICM shows a vertically and horizontally homogeneous ΔT in January and July while the three other models show their largest anomalies in the upper 10 m (particularly SCHISM-ICM), and in the northern oligohaline Bay.

As SLR increases (Figures 9–10 versus Figure 8), both positive and negative anomalies are amplified but the temporal and spatial patterns remain the same. The Bay-averaged change in T is on the order of $\sim \pm 0.08\,^{\circ}\mathrm{C}$, $\sim \pm 0.20\,^{\circ}\mathrm{C}$ and $\sim \pm 0.30\,^{\circ}\mathrm{C}$ for a SLR of +0.17 m, +0.50 m and +1.00 m (respectively), however the negative anomalies tend to be larger in absolute terms than the positive anomalies. The absolute magnitude of the summer anomaly is largest in ChesROMS-ECB, followed by UMCES-ROMS-RCA, CH3D-ICM, and SCHISM-ICM. ΔT reaches $-0.8\,^{\circ}\mathrm{C}$ at the bottom in July in ChesROMS-ECB. Note that these changes in temperature are from simulations where SLR is the sole climate driver considered, and these changes are small relative to those due to atmospheric warming (e.g., *Irby et al.*, 2018).

Bay-wide maps of the change in bottom T in July confirm that the "summer cooling" affects the entire main stem of the Bay, from the Bay's mouth to its northern limit, in all four models (Figures 11–13). There is no clear gradient in ΔT along the main stem of the Bay since anomalies of comparable magnitude can be found in the oligohaline and in the polyhaline. As evident in the figures representing the transects, the temperature anomalies are largest in ChesROMS-ECB and smallest in CH3D-ICM. Of the four models, SCHISM-ICM stands out by exhibiting positive ΔT in the nearshore regions of the Bay, a feature absent from the other three models (and possibly related to inundation processes being only represented in SCHISM-ICM; §2.1).

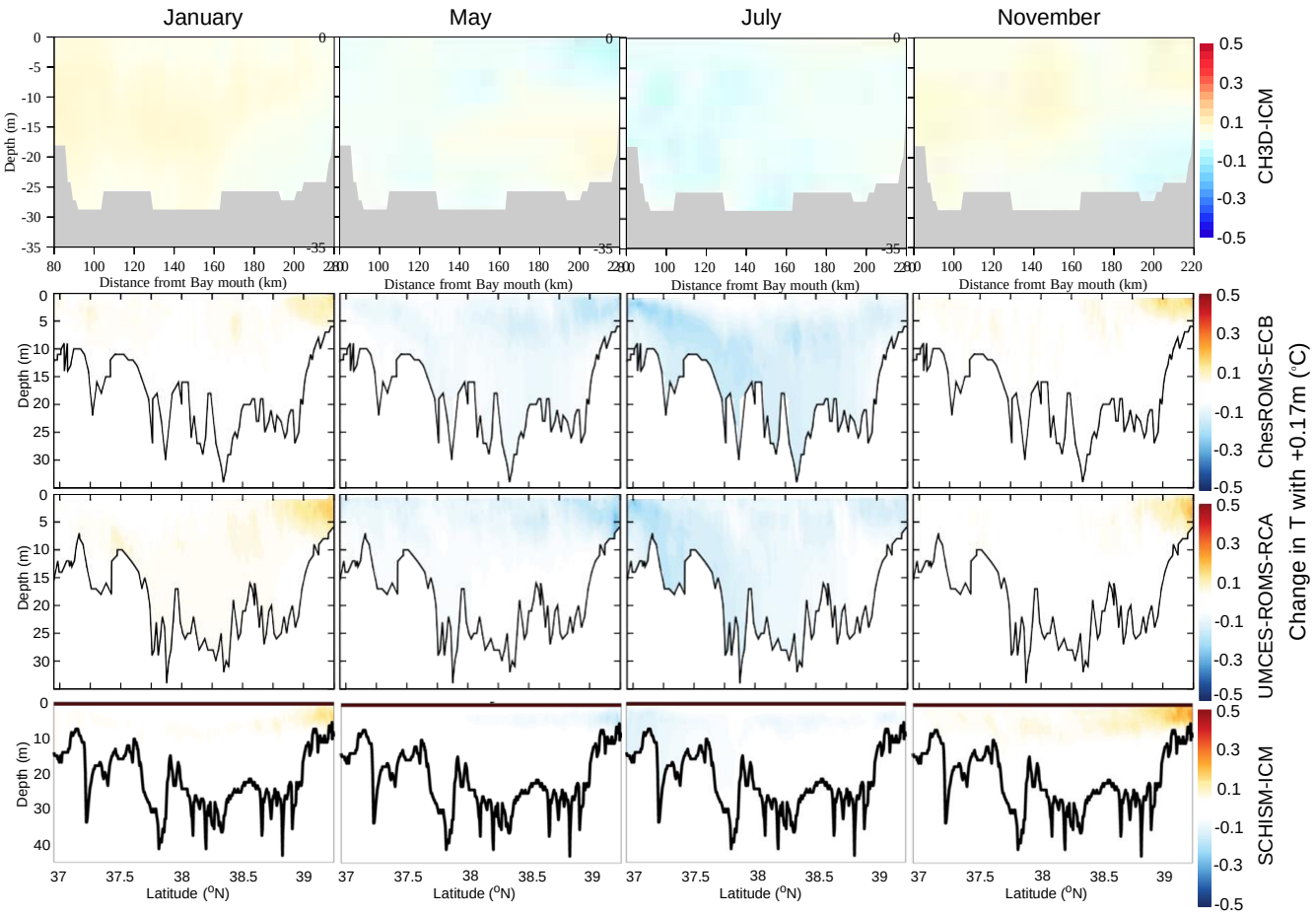

Figure 8: Change in water temperature in response to a sea level rise of +0.17 m (ΔT). The rows represent the four models included in the intercomparison. The columns are months of the year (January, May, July, November). The months selected differ from Figures 2–4 to emphasize the seasonal cycle of ΔT . The figures correspond to the south-north transect depicted in Figure 1e.

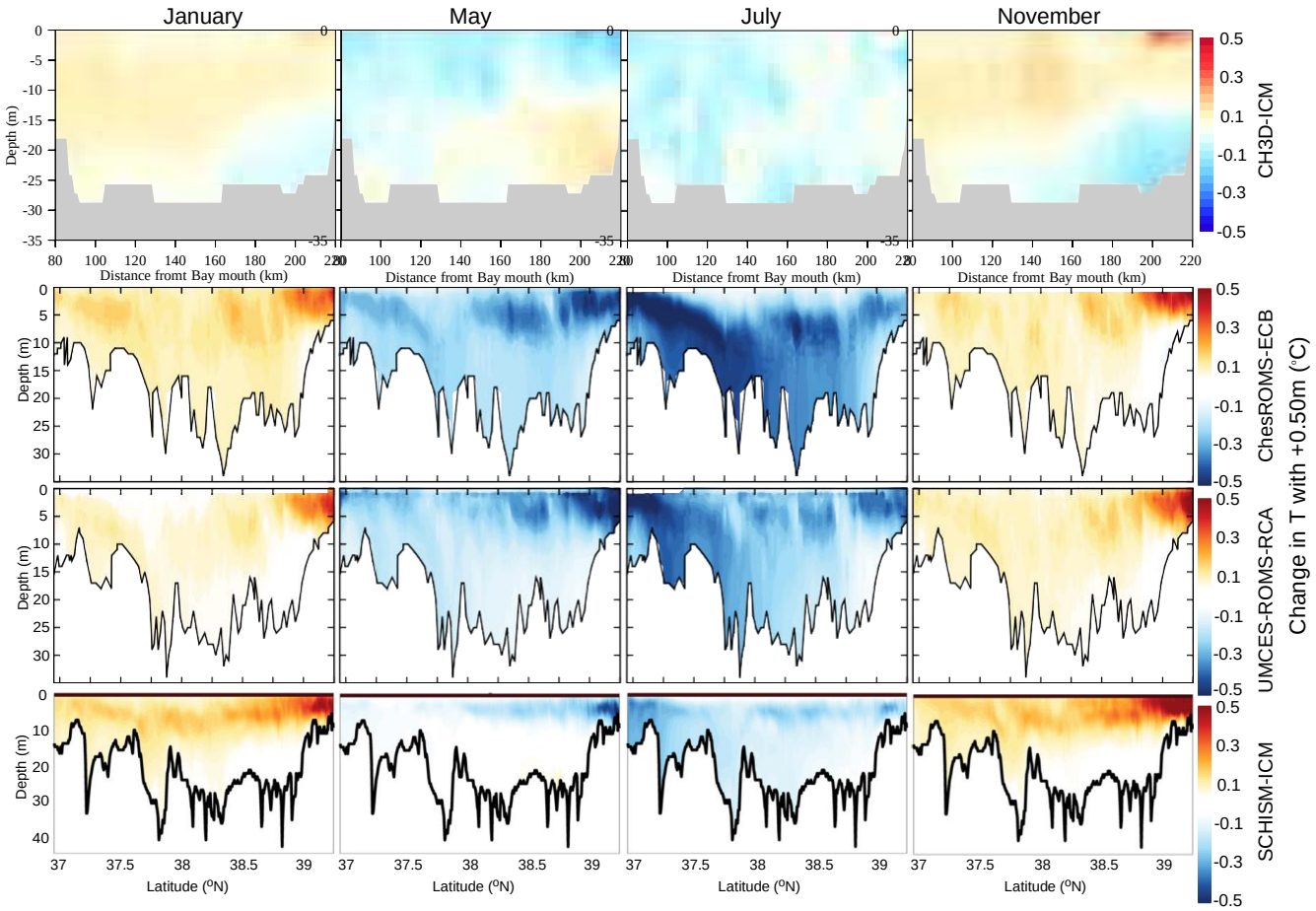

Figure 9: Same as Figure 8 but for a sea level rise of +0.50 m.

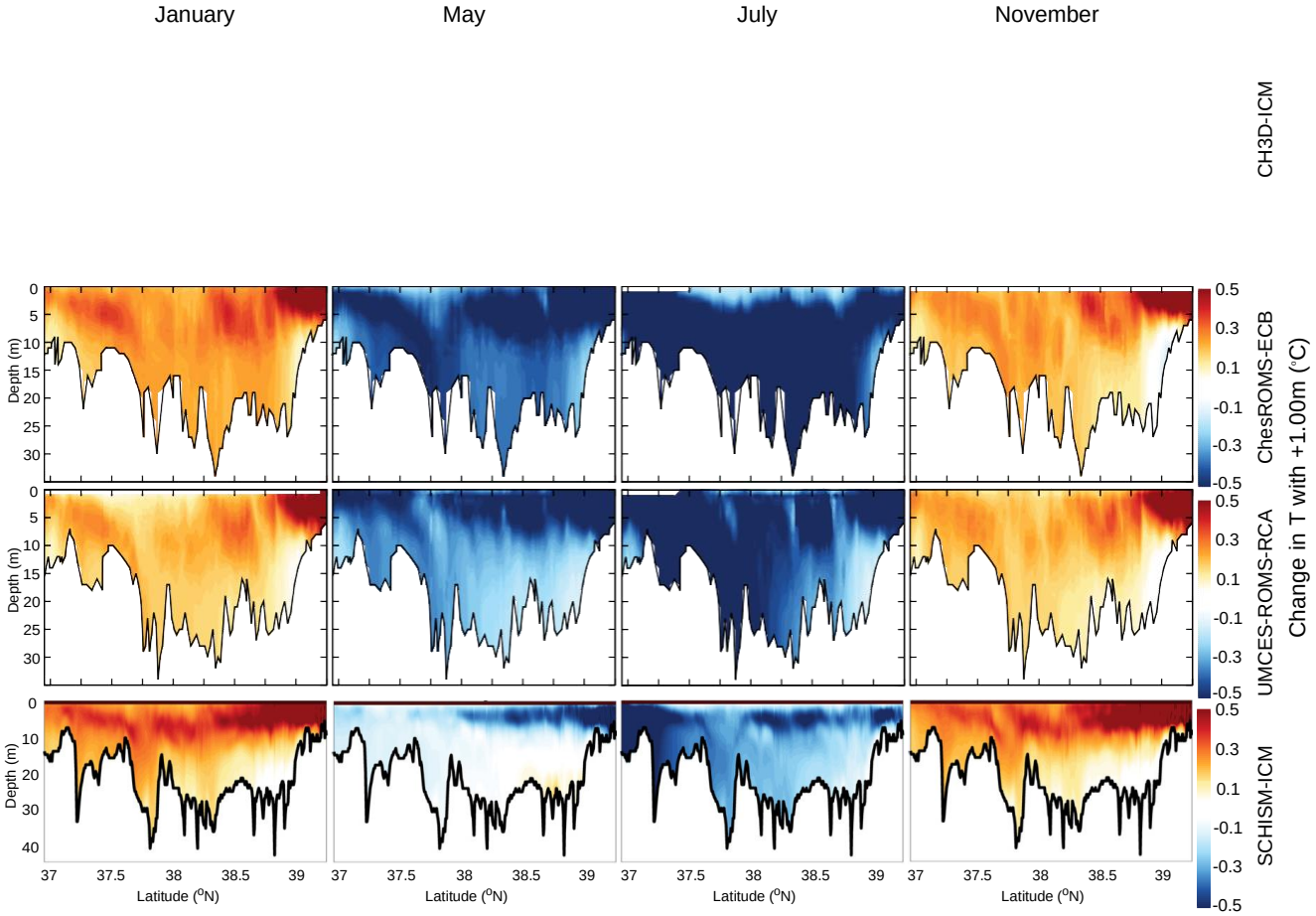

Figure 10: Same as Figure 8 but for a sea level rise of +1.00 m.

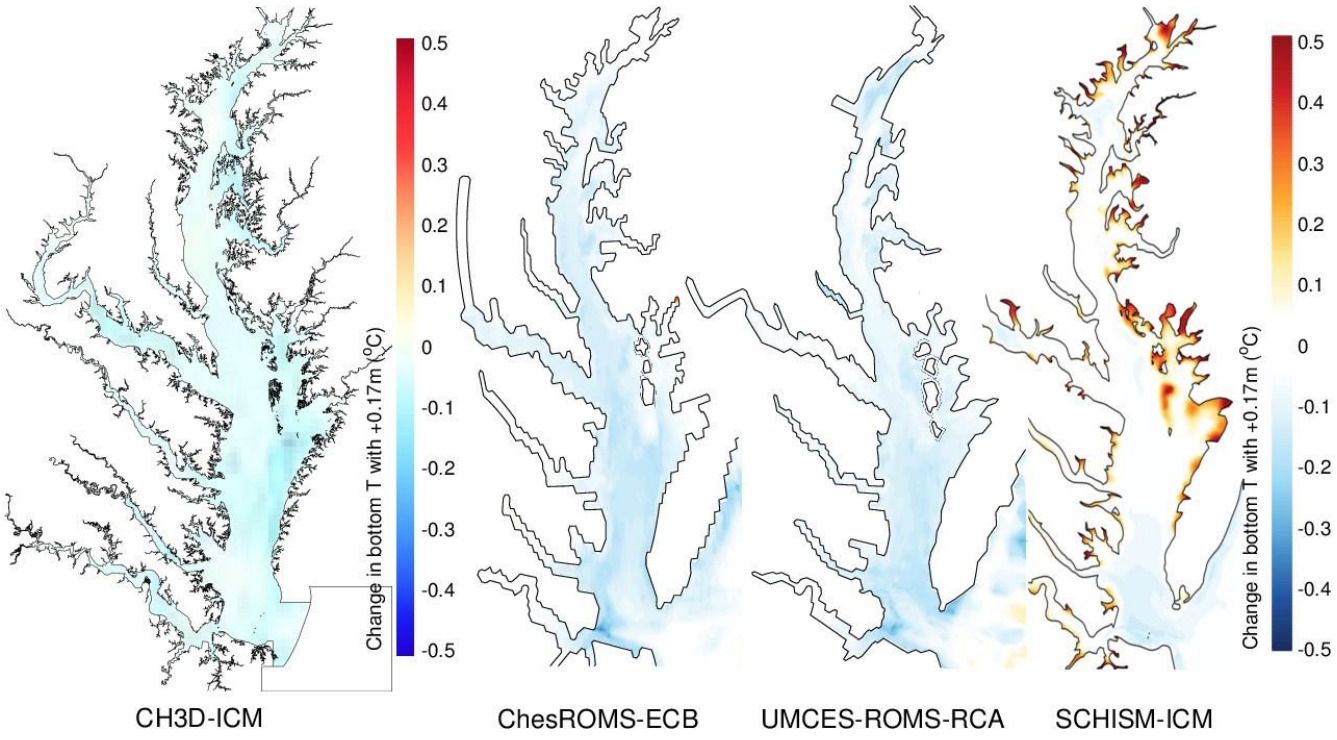

Figure 11: Change in bottom temperature in July in response to a sea level rise of +0.17 m.

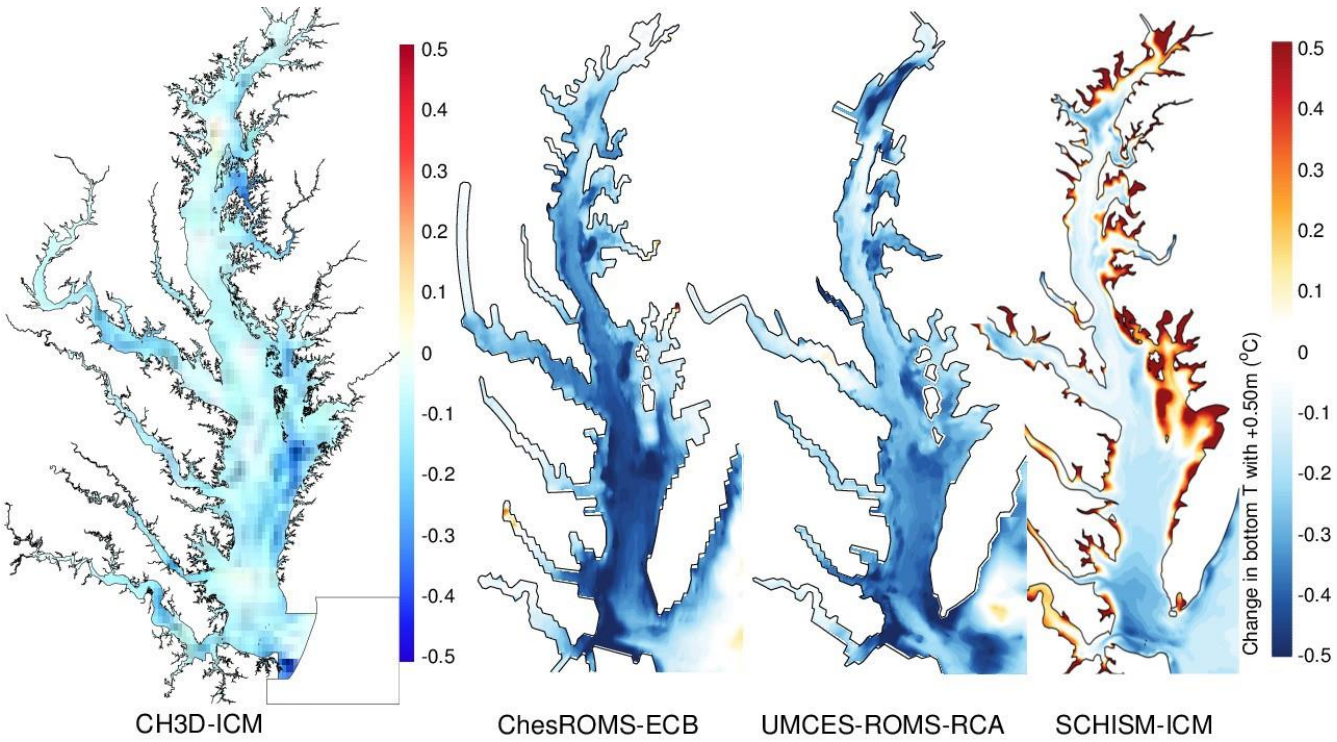

Figure 12: Same as Figure 11 but for a sea level rise of +0.50 m.

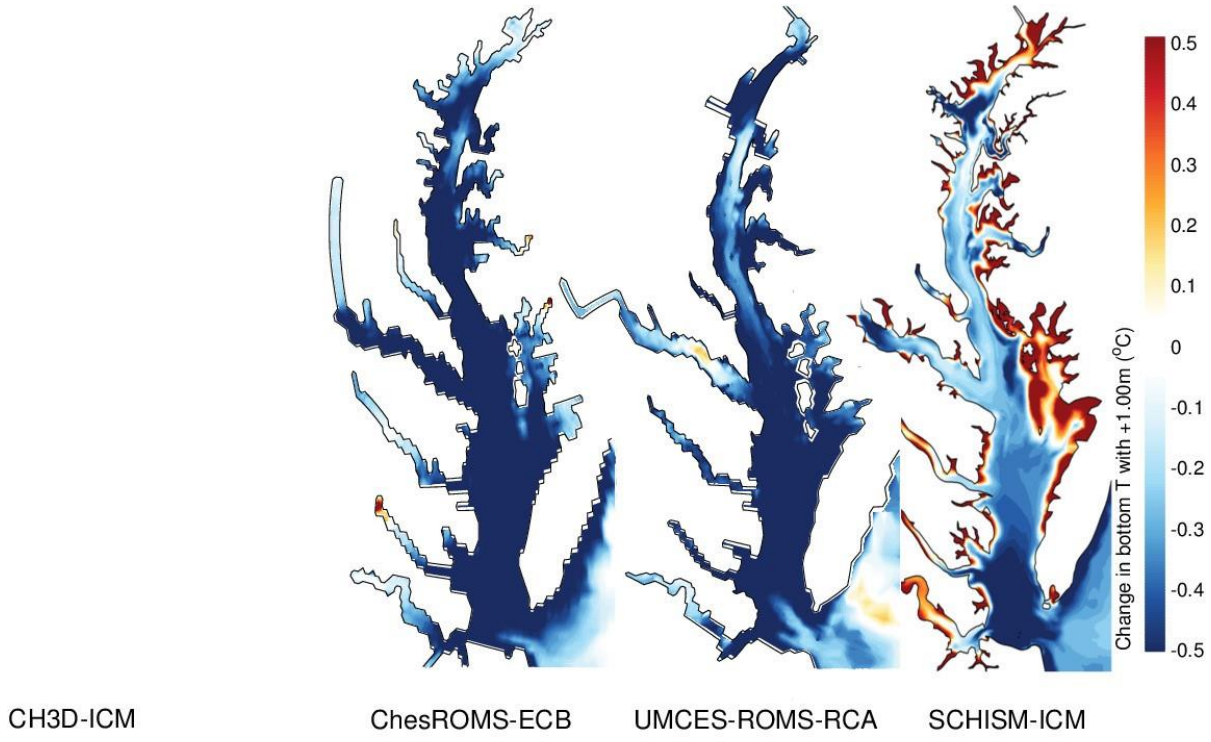

Figure 13: Same as Figure 11 but for a sea level rise of +1.00 m.

3.3 Changes in dissolved oxygen

Dissolved oxygen concentrations both increase and decrease in response to SLR depending on the part of the water column and the period of the year (Figures 14–16). A negative ΔDO is generally apparent in the upper 10 m of the water column while a positive ΔDO is apparent during the summer in the bottom layer of the deep channel (where hypoxia is most prevalent). Both negative and positive anomalies become larger as SL increases, but the spatial and seasonal patterns remain the same.

The four models primarily differ in the magnitude and the duration of the positive DO anomaly in the bottom layer of the deep channel. CH3D-ICM exhibits the largest improvement in bottom DO with positive ΔDO apparent from March to September and values exceeding +0.2 mg L^{-1} in the +0.50 m case (Figure 15). In constrast, UMCES-ROMS-RCA exhibits the smallest improvement in bottom DO, with positive anomalies concentrated in May–July and values in the +0.50 m case of no more than +0.1 mg L^{-1}. ChesROMS-ECB and SCHISM-ICM generally rank between these two models in terms of the magnitude and duration of the positive bottom DO anomaly.

Bay-wide maps of the change in bottom DO in July confirm that the deep areas of the Bay (see Figure 1) are generally associated with either no change in DO (white) or an improvement in DO (warm colors; Figures 17–19). Areas with bottom depth ≤ 10 m typically exhibit a negative ΔDO as expected from the earlier transects. Some exceptions are apparent, however, with complex positive/negative anomalies visible in certain tributaries. CH3D-ICM also suggests large positive ΔDO in the vicinity of Nanticoke River while SCHISM-ICM suggests the opposite. Despite these differences, the presence of a positive ΔDO centered at 38 ° N (mouth of the Potomac River), and extending northward/southward along the deep channel, is a feature suggested by all four models.

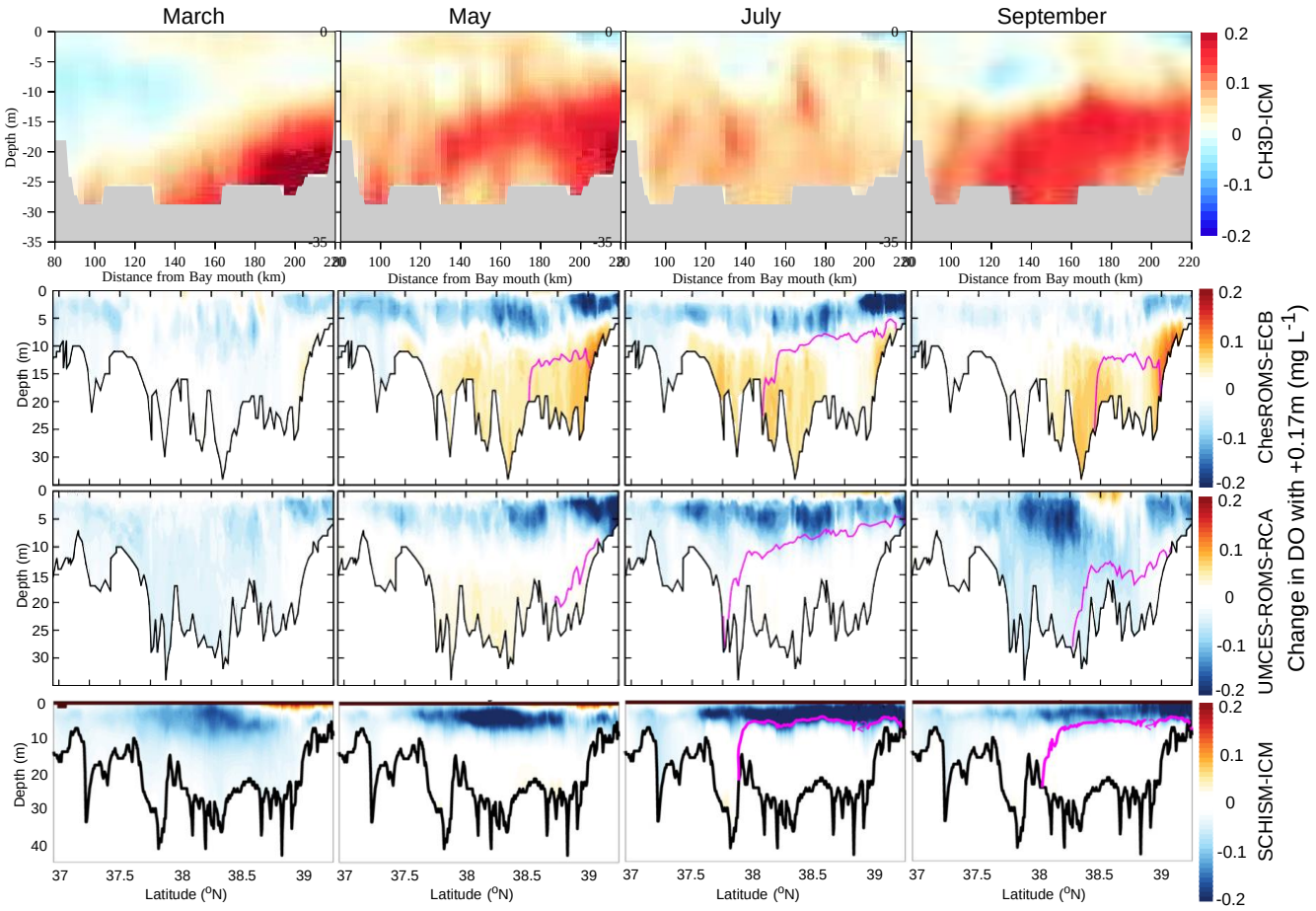

Figure 14: Change in dissolved oxygen concentrations in response to a sea level rise of +0.17 m (ΔDO). The rows represent the four models included in the intercomparison. The columns are months of the year (March, May, July, September). The figures correspond to the south-north transect depicted in Figure 1e. The magenta line is the boundary of the hypoxic zone (DO < 2 mg L^{-1}) in the reference simulation (not shown in the case of CH3D-ICM).

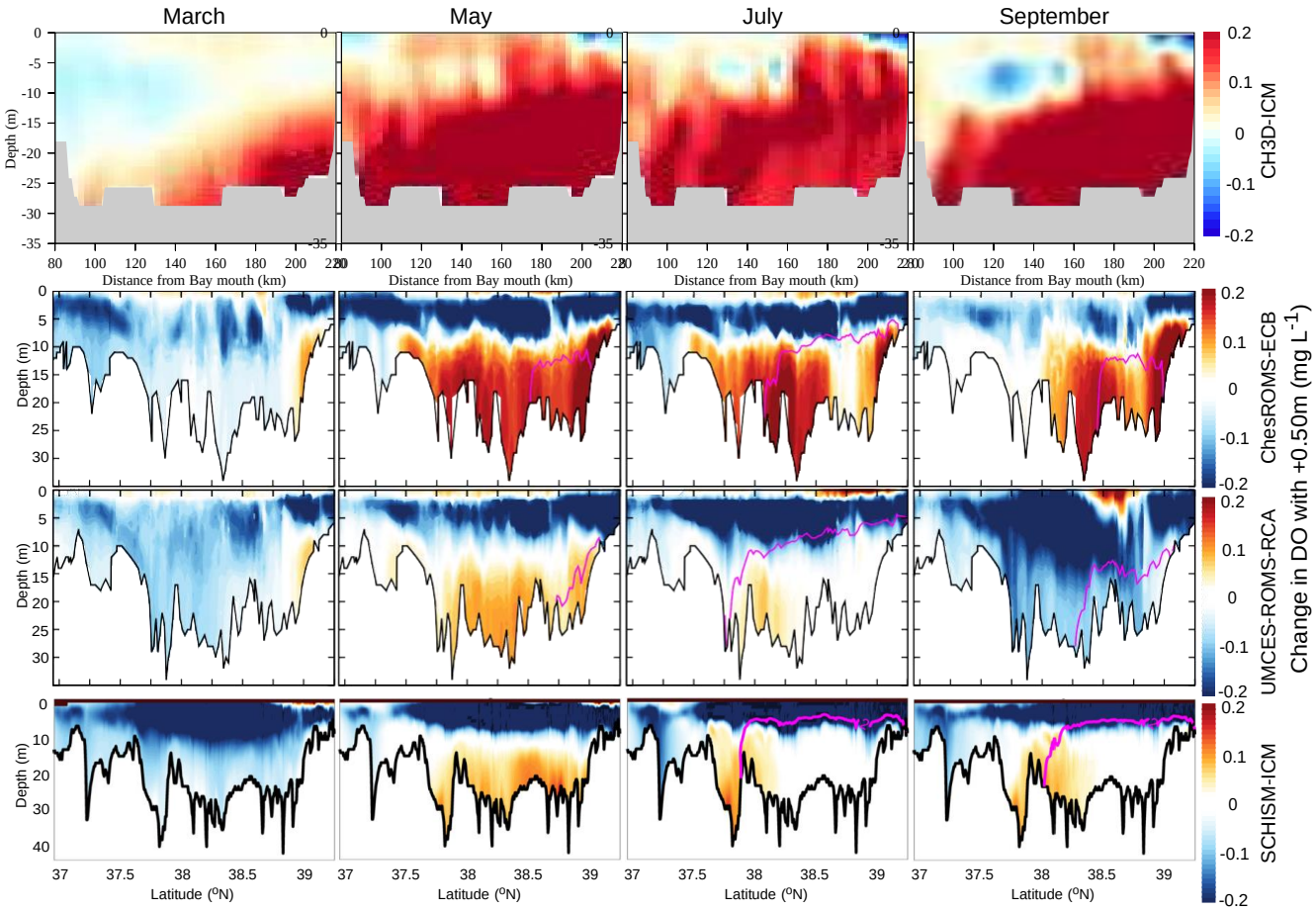

Figure 15: Same as Figure 14 but for a sea level rise of +0.50 m.

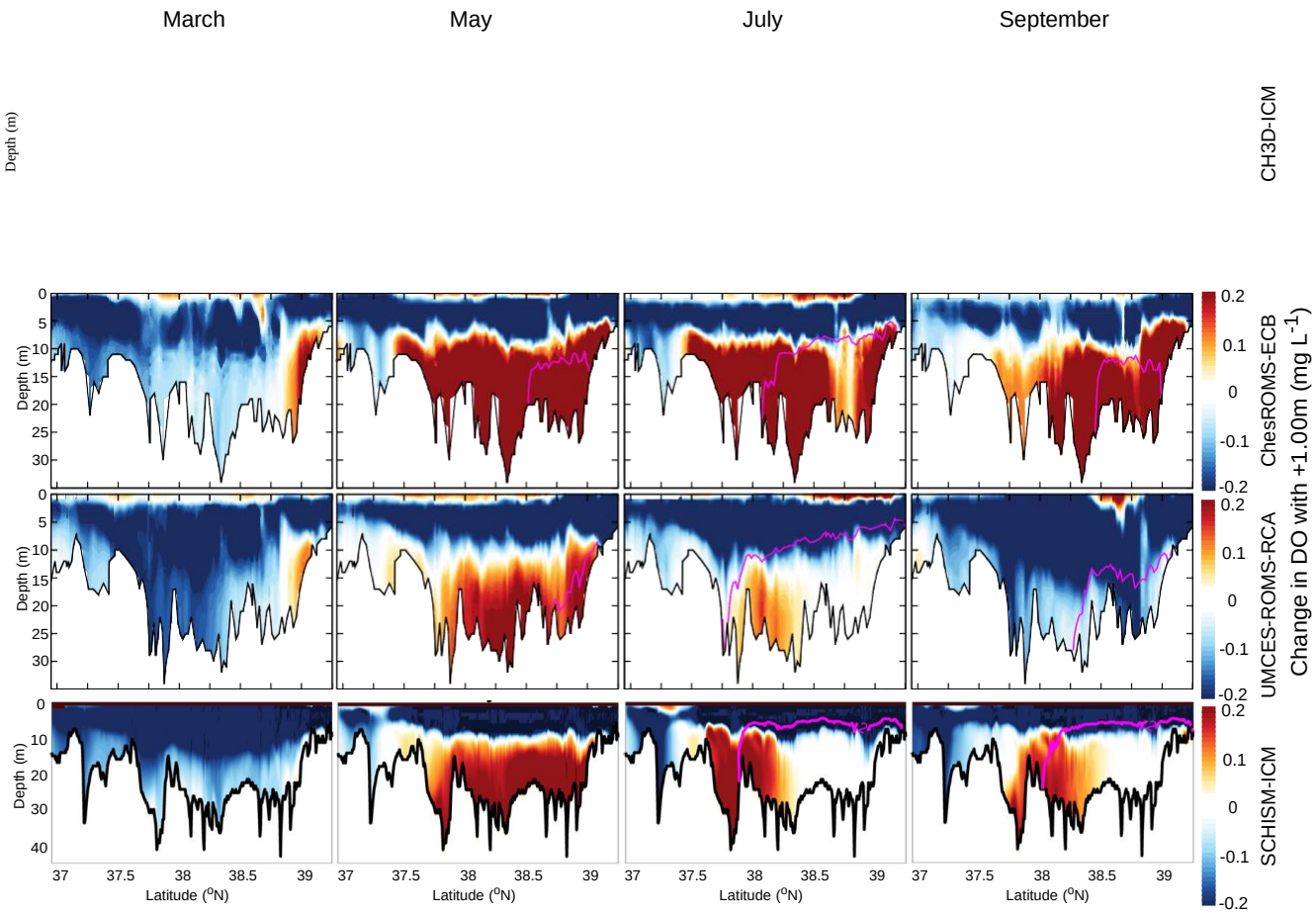

Figure 16: Same as Figure 14 but for a sea level rise of +1.00 m.

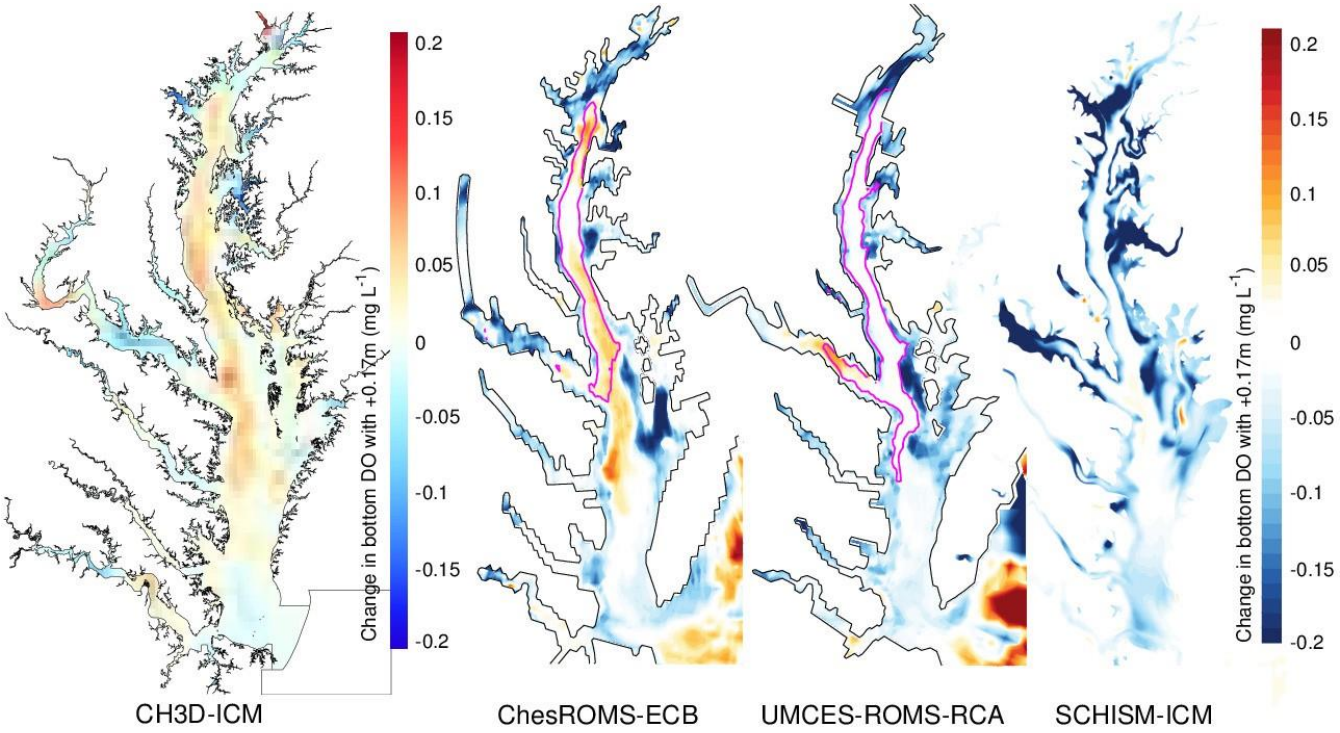

Figure 17: Change in bottom dissolved oxygen in July in response to a sea level rise of +0.17 m. The magenta line is the boundary of the hypoxic zone (DO < 2 mg L^{-1}) in the reference simulation (not shown in the cases of CH3D-ICM and SCHISM-ICM).

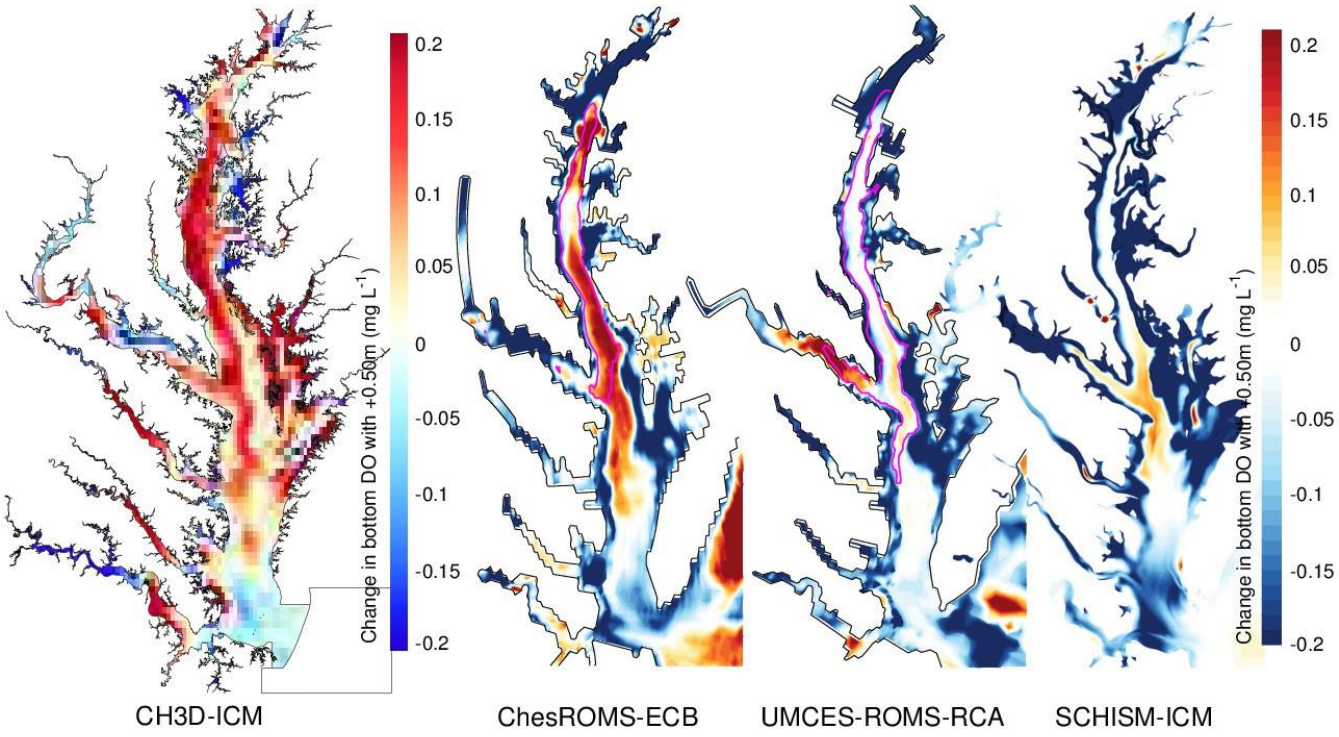

Figure 18: Same as Figure 17 but for a sea level rise of +0.50 m.

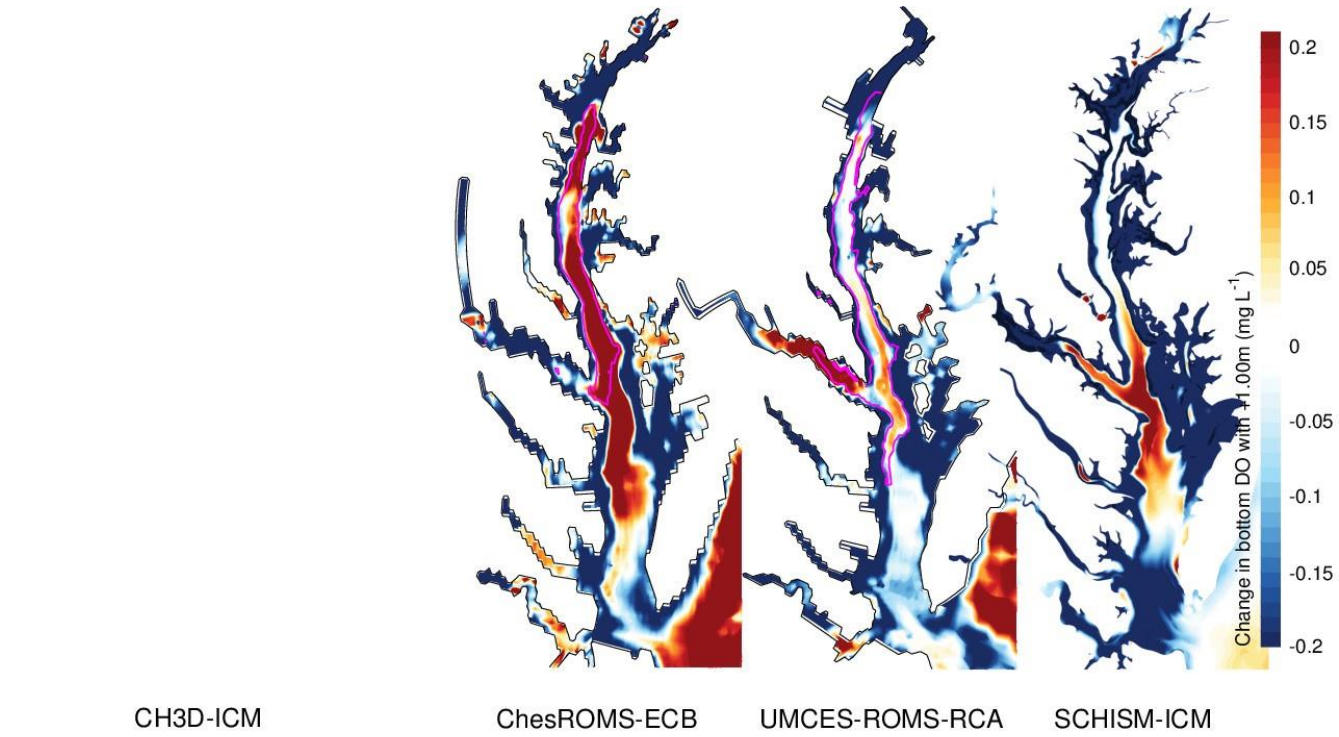

Figure 19: Same as Figure 17 but for a sea level rise of +1.00 m.

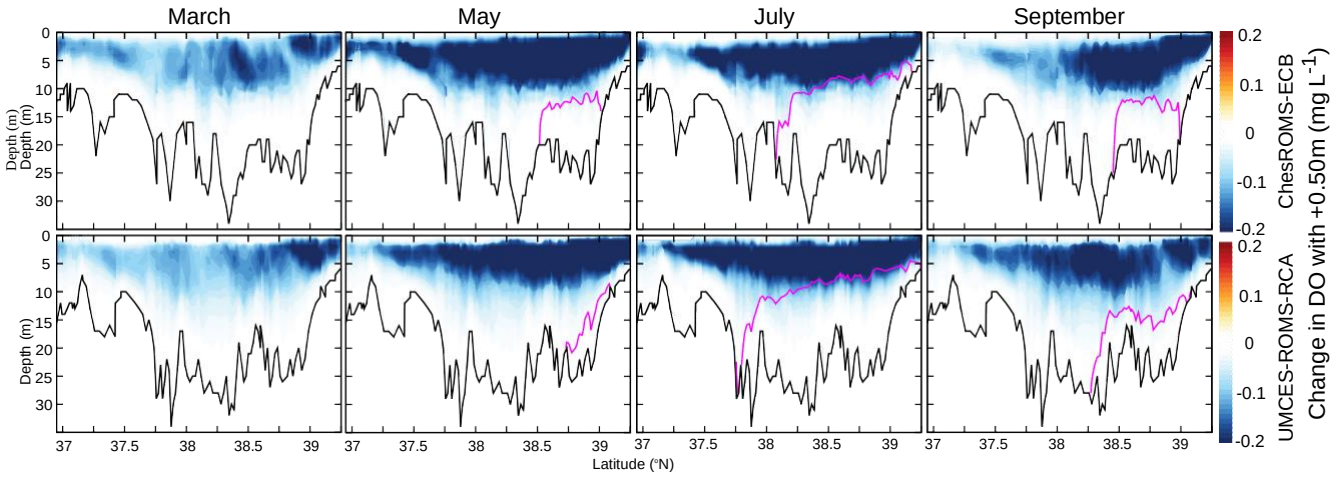

Figure 20: Change in dissolved oxygen concentrations produced by a +0.50 m shift in the oxycline of the reference simulation (Equation 1). The rows represent the models while the columns are months of the year. The figures correspond to the south-north transect depicted in Figure 1e. The magenta line is the boundary of the hypoxic zone (DO < 2 mg L^{-1}) in the reference simulation.

4 Discussion

4.1 Contribution of water column stretching to ΔDO

A key impact of increasing sea level is the reduced oxygen concentrations in the upper 10 m of the water column (Figures 14–19). Because DO generally decreases with depth, an upward shift in the position of the oxycline (*i.e.*, the equivalent of the thermocline but for DO) will result in a negative DO anomaly. To quantify this contribution, the DO fields of the reference simulation were artificially shifted upward according to Equation 1 and assuming a ΔSL of +0.50 m. The calculation focuses on ChesROMS-ECB and UMCES-ROMS-RCA, the two models for which results are directly available for analyses.

The upward shift of the DO field generates, by itself, negative DO anomalies that are very similar to those of the +0.50 m case (compare Figures 15 and 20). The anomalies of the two figures match in terms of spatial distribution and magnitude, particularly during the summer period (May–July) when the DO field is most stratified and the effect of the vertical shift is expected to be the strongest. The good correspondence between the two sets of results indicates that the water column stretching (Equation 1) can account for the reduced surface oxygen concentrations due to SLR (apparent in Figures 14–19).

4.2 Contribution of DO_{sat} to ΔDO

The "summer cooling" of water temperatures due to SLR (Figures 8–13) could potentially contribute to the improvement in bottom DO (Figures 14–19) by increasing DO_{sat}. In July, the models suggest for the +0.50 m case a temperature decrease on the order of ~ −0.3 °C and a salinity increase of ~ +0.7 psu. Assuming a reference temperature of 25 °C and a reference salinity of 20 psu, the changes in temperature and salinity are equivalent to ΔDO_{sat} = +0.04 mg L^{-1} and ΔDO_{sat} = −0.03 mg L^{-1}, respectively. The changes in temperature and salinity thus tend to compensate each other to produce a small net change in oxygen saturation and oxygen concentrations.

To illustrate this point further, the changes in DO_{sat} were computed using the simulated ΔT and ΔS

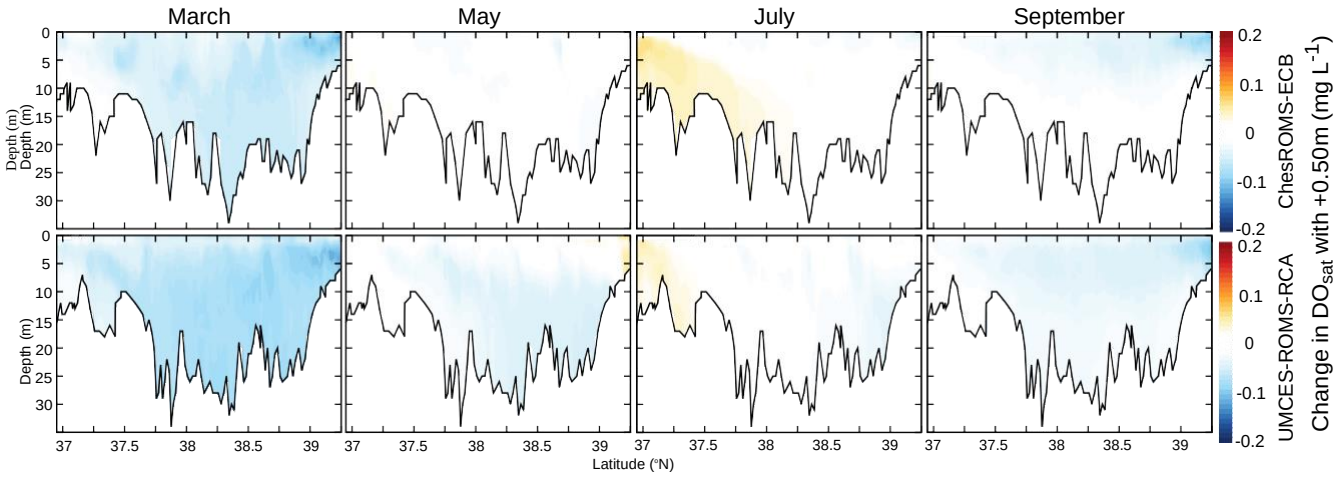

Figure 21: Change in DO_{sat} in response to a sea level rise of +0.50 m (ΔDO_{sat}). The figure should be compared to Figure 15. The rows represent the models while the columns are months of the year. The figures correspond to the south-north transect depicted in Figure 1e.

of the +0.50 m case (Equation 2). The calculation focuses on ChesROMS-ECB and UMCES-ROMS-RCA, the two models for which outputs are directly available for analyses. ΔDO_{sat} is mostly white (no net change) during July (Figure 21), with a maximum value of +0.04 mg L^{-1} where ΔT is most negative (Figure 9). We note that +0.04 mg L^{-1} is considerably smaller than the DO anomalies simulated by the models during the same month (Figure 15). During the rest of the year, the effect of salinity dominates and produces negative ΔDO_{sat} values. Overall, the calculation indicates that physically-driven changes in the solubility of oxygen cannot account for the improvement in summer bottom DO visible in Figures 14–19.

4.3 Contribution of respiration to ΔDO

To explore the mechanisms behind the positive bottom DO anomaly (§3.3), an oxygen budget for the bottom layer of the deep channel is computed:

$$\frac{\partial}{\partial t} \qquad \mathrm{DO}\, dV \approx \mathit{Transport} + \mathit{Respiration}, \tag{4}$$

where the left-hand side is the temporal change in the total DO content of the bottom layer (in kg-O_2 s^{-1}), transport represents the net effect of DO advection and DO diffusion, and respiration is the sum of water-column respiration and sediment oxygen demand. Note that oxygen production does not appear in the budget as it focuses on the bottom layer (outside of the euphotic zone). This budget was used in *Li et al.* (2015) and *Li et al.* (2016) albeit with a different grouping of the terms on the right-hand side. As in the earlier studies, the bottom layer of the deep channel is defined as a fixed control volume (of size 8 km^3) encompassing all the waters below $z = -10$ m in the main stem of the Bay between 37.45°N and 39.2°N (Figure 22a).

The budget is first computed from the reference simulation of the two models for which outputs are directly available for analyses (ChesROMS-ECB and UMCES-ROMS-RCA). In both models, transport and respiration largely mirror each other throughout the year, with a small net effect represented by the temporal derivative (Figure 22b). Note that respiration does not depend on DO transport (but rather on

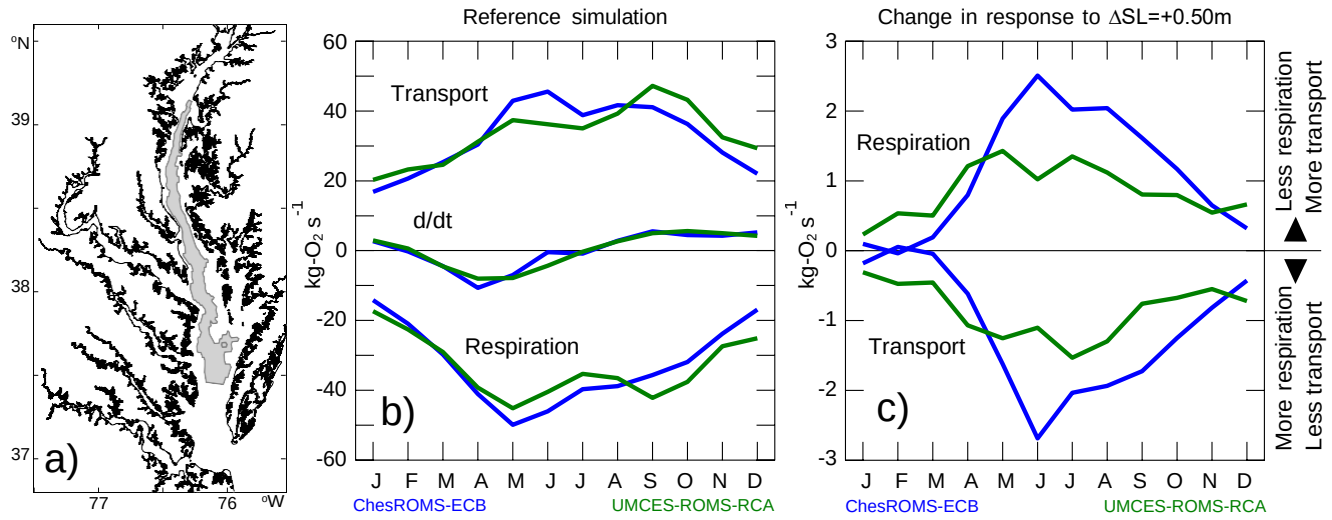

Figure 22: Oxygen budget for the bottom layer of the deep channel. (a) Geographical extent of the control volume considered in the budget (gray shading; similar to *Li et al.* (2016)). (b) Budget terms for the reference simulations of ChesROMS-ECB and UMCES-ROMS-RCA. (c) Change in the budget terms in response to a sea level rise of +0.50 m.

organic matter concentrations and water temperature) and thus it is DO transport that is following the magnitude of respiration throughout the year. A rationale for this behavior is that respiration determines the spatial gradients of DO on which advection and diffusion depend. Overall, the transport and respiration are largest (in absolute values) between May and September with UMCES-ROMS-RCA exhibiting a slightly broader maximum than ChesROMS-ECB. The temporal derivative is negative from February to July, and positive from August to January as the deep channel recovers from summer hypoxia. Note that the annually-averaged respiration term of the two models are within 2% of each other in the reference simulations (32.4 and 33.2 g-O2 s^{-1} for ChesROMS-ECB and UMCES-ROMS-RCA, respectively).

It is instructive to examine how these budget terms are modified by the introduction of SLR (+0.50 m case, Figure 22c). Both models suggest that there is less respiration with SLR, *i.e.* that SLR makes this term less negative in Equation 4. On average over the year, the change amounts to 3.5% (ChesROMS-ECB) or 2.5% (UMCES-ROMS-RCA) of the respiration from the reference run. During May–July, the change amounts to 5% (ChesROMS-ECB) or 3% (UMCES-ROMS-RCA) of the respiration from the reference run. The vast majority of the change is in the water-column respiration rather than the sediment oxygen demand. The two models also indicate that the transport of DO decreases in response to SLR, and this change largely mirrors the change in respiration. Therefore, the changes in transport cannot account for the increase in the deep channel DO in summer since the change is in the wrong direction. Rather, it is the decrease in respiration that is responsible for the positive ΔDO.

Although the two models agree in the direction of the changes in respiration and transport, the magnitude of these changes differs between the models (Figure 22c). Between June and September, the changes in ChesROMS-ECB are a factor 1.9 larger than in UMCES-ROMS-RCA. The seasonality of these changes, defined as the annual maximum divided by the annual mean, is also more pronounced in ChesROMS-ECB than in UMCES-ROMS-RCA (2.3 and 1.7, respectively). Ultimately, these differences between the models' respiration is what causes the differences in the magnitude and duration of the positive ΔDO in the bottom layer of the deep channel.

4.4 Variables affecting respiration in the models

Considering that a decrease in the respiration of the bottom layer is what causes the improvement in the bottom DO of the deep channel (§4.3), we examine in this section the variables affecting this process. Respiration in the deep channel of the Bay is dominated by the water-column component (*Li et al.*, 2015, 2016) which, in turn, depends on organic matter concentrations and on water temperature T via temperature-dependent respiration rates. In ChesROMS-ECB, respiration within the water column is modulated by the function $\exp(0.0742\,T)$ which is equivalent to a Q_{10} index of 2.1 (*Lomas et al.*, 2002):

$$Q_{10} \equiv \frac{rate(T + 10^{\circ}\mathrm{C})}{rate(T)}, \tag{5}$$

where Q_{10} represents the factor increase for a 10°C increase in water temperature. CH3D-ICM assumes a similar temperature dependence of the form $\exp[0.069\,(T - 20^{\circ}\mathrm{C})]$ (*Cerco et al.*, 2010) or, equivalently, $0.252\exp(0.069\,T)$. This temperature dependence corresponds to a Q_{10} index of 2.0 and is thus similar to that of ChesROMS-ECB. In UMCES-ROMS-RCA, respiration of organic matter in the water column is modulated by temperature as $\theta^{(T-20^{\circ}\mathrm{C})}$ with θ varying between 1.02 and 1.08 depending on the respiration processes (*Testa et al.*, 2014).

These differences in the temperature dependence of the models are illustrated in Figure 23a. The rates in the figure are normalized by their value at $T = 20^{\circ}$C to emphasize the sensitivity (defined by the slope of the curves) to a change in water temperature. The value $\theta = 1.08$ is comparable to the temperature-dependence of ChesROMS-ECB, while $\theta = 1.02$ is approximately 3 times less sensitive to a change in temperature. A "summer cooling" of $\Delta T \approx -0.4^{\circ}$C (case +0.50 m, §3.2) is equivalent to a 3% slower respiration rate in ChesROMS-ECB and in UMCES-ROMS-RCA (assuming $\theta = 1.08$). We note that this reduction is comparable to the decrease in bottom layer respiration projected by the ROMS models for the same SLR case (§4.3). In other words, the "summer cooling" combined with the temperature-dependent rates can account for the decrease in bottom-layer respiration of the ROMS models.

Another variable affecting the respiration in the bottom layer is the amount of organic matter entering this layer. We estimate this variable by integrating the primary production of the models vertically and horizontally over the control volume representing the deep channel of the Bay (Figure 22a). The production is then converted to oxygen units using the stochiometric conversions of the models (*Feng et al.*, 2015; *Testa et al.*, 2014). The production of the two ROMS models responds differently to sea level rise (case +0.50 m, Figure 23b). ChesROMS-ECB suggests an increase in January–March, and a decrease during the summer months (May–September). In contrast, UMCES-ROMS-RCA suggests either no change (April–May) or a moderate increase in production (particularly around August). Focusing on the period May–September, these changes represent a 2.6% decrease (ChesROMS-ECB) and a 2.0% increase (UMCES-ROMS-RCA) relative to the production of the reference runs.

The changes in production in response to SLR can be rationalized to a certain extent by examining the temperature dependence of phytoplankton production (Figure 23c). Again, the figure illustrates the maximum production rates normalized by their value at $T = 20^{\circ}$C. In the ChesROMS-ECB simulations, the maximum production rate is constant for $T < 16.5^{\circ}$C and, otherwise, is modulated by the function $\exp(0.078\,T)$. The coefficient 0.078 is equivalent to a Q_{10} index of 2.18 (*Lomas et al.*, 2002). The constant value for $T < 16.5^{\circ}$C acknowledges the fact that production rates are relatively insensitive to temperature in this range (*Lomas et al.*, 2002). With this temperature dependence, a summer cooling of -0.4°C (+0.50 m case for ChesROMS-ECB; Figure 9) would produce a 3% decrease in the maximum production rate of ChesROMS-ECB (consistent with Figure 23b).

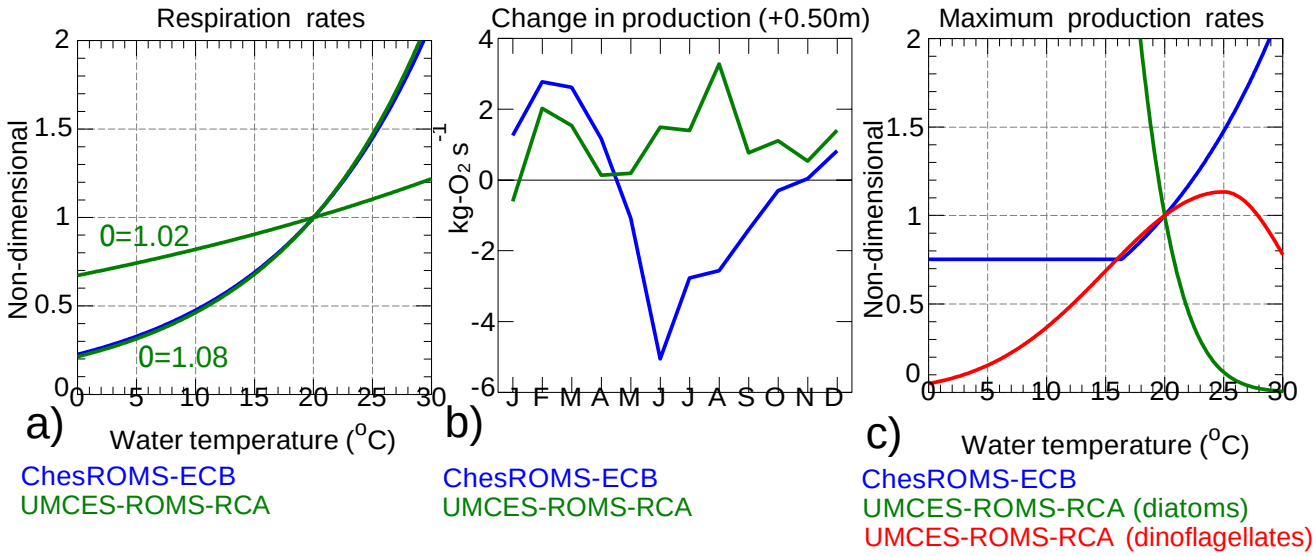

Figure 23: Temperature dependence of the models and changes in production in response to SLR. (a) Temperature dependence of respiration processes. The rates are normalized by their value at a temperature $T = 20\,^{\circ}\mathrm{C}$. (b) Changes in oxygen production for the case $\Delta SL = +0.50$ m. The production is integrated vertically (surface to bottom) and horizontally over the control volume (Figure 22a). (c) Same as (a) but for the maximum primary production rate. The rates are normalized by their value at a temperature $T = 20\,^{\circ}\mathrm{C}$. In the case of the diatoms group (green curve), the function reaches a maximum at $T = 7\,^{\circ}\mathrm{C}$ (not visible in the figure).

In UMCES-ROMS-RCA, two phytoplankton groups (diatoms and dinoflagellates) are represented with distinct temperature dependences of the form $\exp\left(-\alpha\,(T - T_{\mathrm{opt}})^2\right)$ (*Testa et al.*, 2014). Such bell-shaped functions reach a maximum at $T = T_{\mathrm{opt}}$ and gradually decrease away from T_{opt}. The diatoms' production rate is maximum at $7\,^{\circ}\mathrm{C}$ while dinoflagellates' production is maximum at $25\,^{\circ}\mathrm{C}$ (Figure 23c). The net effect of a "summer cooling" is unclear as the two groups would react in opposite ways (an increase for diatoms and a decrease for dinoflagellates) assuming $7 < T < 25\,^{\circ}\mathrm{C}$. At temperatures higher than $25\,^{\circ}\mathrm{C}$, a cooling would increase the production rate of dinoflagellates. These aspects are difficult to constrain considering that only information about the total production is available.

Regardless of what causes these changes in production, they are very likely to contribute to the differences in the impacts of SLR on DO concentrations (see §3.3). In ChesROMS-ECB, the decrease in summer production and respiration rates both contribute to less respiration in the bottom layer (and thus an increase in bottom DO). In UMCES-ROMS-RCA, the increase in production around August would act in opposition to the temperature-driven decrease in respiration rates. This contrast between the models likely contributes to the differences in the magnitude/duration of the increases in bottom DO due to SLR (§3.3). It also points to the need for a careful selection of model parameter values, particularly when studying relatively small effects such as those caused by SLR.

4.5 Changes in hypoxic volumes

It was noted in §3.3 that all four models show some improvement in bottom DO in the deep channel during May–July in response to SLR (Figures 14–19). Taken by itself, this result would suggest that the hypoxic volume, defined as the volume of water with DO $< 2\,\mathrm{mg\ L^{-1}}$, would decrease in response to

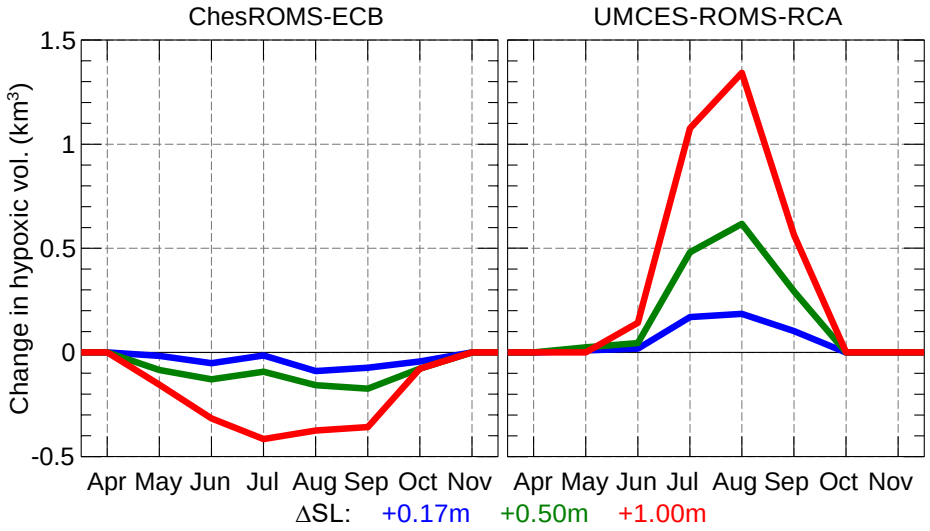

Figure 24: Change in the volume of hypoxic water (DO < 2 mg L^{-1}) in response to sea level rise.

SLR. However, it is instructive to examine where the boundary of this hypoxic zone lies in relation to the positive/negative ΔDO. The vertical extent of the hypoxic zone in July reaches depths as shallow as 5 m (see the magenta line in Figures 14–16). The boundary is thus high enough in the water column to lie in the zone of negative ΔDO, which is particularly apparent for UMCES-ROMS-RCA and for SCHISM-ICM. In such cases, the hypoxic boundary will expand upward with SLR and contribute to an increase in hypoxic volume.

Similarly, the horizontal extent of the hypoxic zone in July straddles the contour line of ΔDO = 0 and often ventures into areas with ΔDO < 0 (magenta line in Figures 17–19). Once again, this is particularly apparent in the case of UMCES-ROMS-RCA. The hypoxic zone will thus expand horizontally with SLR in these parts of the main stem, irrespective of the presence of positive ΔDO at the bottom of the deep channel. In contrast, the hypoxic boundary of ChesROMS-ECB typically lies in regions of ΔDO ≥ 0.

These small differences in the position of the hypoxic boundary have a profound impact on the change in hypoxic volumes in response to SLR (Figure 24). ChesROMS-ECB suggests a smaller volume between May and October, while UMCES-ROMS-RCA suggests a larger volume between June and September. This contrasted response is obtained even though both models exhibit some improvements in bottom DO in the deep channel (Figures 17–19), and is due to the fact that the change in volume mostly depends on where the hypoxic boundary lies in relation to the positive/negative DO anomalies.

This result has potential implications for the study of ecosystems within the Bay. It suggests that Bay-wide metrics such as hypoxic volume would not necessarily reflect local changes caused by long-term climate trends. Instead, both the magnitude and spatial distribution of DO anomalies should be considered when evaluating changes in habitat suitability.

4.6 Linearity of the changes caused by SLR

The changes in salinity, temperature and dissolved oxygen (Figures 2–16) are generally amplified with increasing SLR, but the linearity of these changes has not been examined in the earlier sections. For this purpose, we select one location along the south-north transect (Station CB5.2 of the Water Quality Monitoring Program; 38.14 ° N, 76.23 ° W) representative of the deep channel where a positive bottom DO

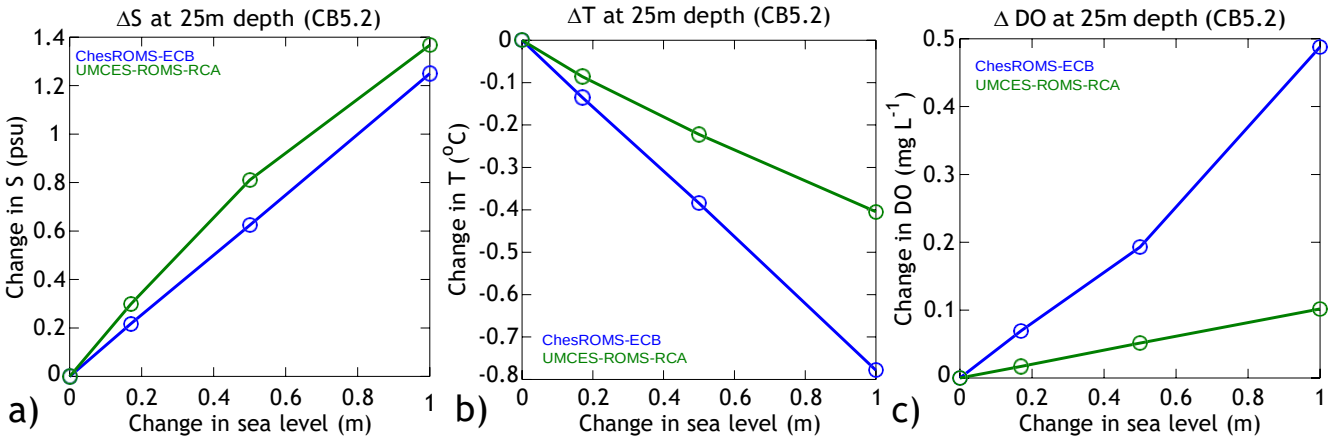

Figure 25: Linearity of the changes caused by SLR at a station representative of the deep channel during the month of peak hypoxia (July). (a) Change in salinity near the bottom of Station CB5.2 (38.14 ◦ N, 76.23 ◦ W) as a function of SLR. (b) Same as (a) but for water temperature. (c) Same as (a) but for dissolved oxygen.

is apparent in all four models. More specifically, we select a depth horizon close to the seabed ($z = -25$ m) and focus on the month of July (when hypoxia is at its annual maximum). The analysis also focuses on the two models for which outputs are directly available for such analyses (ChesROMS-ECB and UMCES-ROMS-RCA).

The two model projections are quantitatively very close in the case of salinity (Figure 25a). The three SLR experiments roughly follow a straight line, indicating that changes in salinity are linear as SL increases. In the case of temperature, ChesROMS-ECB suggest a stronger "summer cooling" than UMCES-ROMS-RCA (as mentioned in §3.2) and this difference between the two models grows with SLR. Nevertheless, the three experiments of a given model form a quasi straight line. For DO concentrations, ChesROMS-ECB is far more sensitive to SLR than UMCES-ROMS-RCA (§3.3) but the three experiments mostly suggest, once again, a linear increase with SLR. The last data point of ChesROMS-ECB (case +1.00m) could indicate a slight non-linear behavior but additional experiments would be required to confirm this possibility. Overall, the experiments suggest that the model results for S, T, and DO can be linearly interpolated to other values of SLR within the range $0 < \Delta SL < 1$ m without a loss of information.

5 Conclusions

The key outcomes from the study are:

- There is considerable agreement between ChesROMS-ECB, UMCES-ROMS-RCA and SCHISM-ICM in how salinity changes in response to SLR (§3.1); however, CH3D-ICM produces smaller salinity increases. In all four models, salinity increases throughout the Bay and throughout the water column with little seasonality. The changes become larger as sea level continues to rise, but their spatial distributions remain similar. The models do not suggest an appreciable change in the top-to-bottom haline stratification with SLR. The model projections are quantitatively close to those of *Hong and Shen* (2012).

- The models agree that SLR, in the absence of other drivers of climate change, produces slightly warmer water temperatures in November–January and slightly cooler water temperatures in May–

July (§3.2). These changes again become larger as sea level continues to rise but their spatial distributions remain similar. The models exhibit variations in the vertical structure of ΔT (either concentrated in the upper 10 m or vertically homogeneous). SCHISM-ICM distinguishes itself from the three other models by exhibiting positive ΔT at the bottom in July in the shallowest parts of the Bay.

- The four models agree that SLR decreases DO concentrations in the upper 10 m and increases bottom DO at least in parts of the deep channel in May–July (§3.3). These changes are larger as sea level continues to rise but the seasonal and spatial patterns remain similar. The models differ in the magnitude and duration of the positive bottom DO anomaly.

- The vertical profiles of DO are uplifted by SLR and this accounts quantitatively for the negative ΔDO in the upper part of the water column (§4.1). The positive ΔDO apparent in the bottom layer of the deep channel in the summer cannot be explained by changes in water solubility (§4.2).

- Changes in the advection/diffusion of DO in response to SLR cannot account for the increases in DO in the bottom layer of the deep channel (§4.3). Instead, both ROMS models point toward a decrease in bottom-layer respiration as the cause of the increases in bottom DO.

- The slightly cooler water temperatures during summer, combined with the temperature-dependent respiration rates of the models, can account for the $\sim$ 3% decrease in bottom layer respiration of the ROMS models (§4.4). Differences in temperature-dependent rates and primary production are likely responsible for UMCES-ROMS-RCA exhibiting a smaller decrease in bottom-layer respiration (and, in turn, a smaller increase in bottom DO) than ChesROMS-ECB (§4.4). These results point to the need for a careful selection of model parameters, particularly when studying relatively small effects such as those caused by SLR.

- Changes in hypoxic volumes in response to SLR are a poor indicator of changes in DO concentrations within the deep channel (§4.5). The boundary of the hypoxic zone (isosurface of DO = 2 mg L^{-1}) often lies in shallow areas where the models produce decreases in DO. In these cases, the hypoxic volume will expand with SLR, regardless of the presence/absence of increases in DO within the deep channel. We strongly recommend that consistent metrics be used when comparing model studies of hypoxia.

References

Brady, D. C., J. V. DePinto, S. C. Chapra, D. M. Di Toro, M. A. M. Friedrichs, M. W. Gray, T. Jordan, and M. Xia (2018), Chesapeake Bay Water Quality and Sediment Transport Model (WQSTM) review, *Tech. rep.*, Scientific and Technical Advisory Committee (STAC), publication 18-002, Edgewater, MD.

Cerco, C. F., S. C. Kim, and M. R. Noel (2010), The 2010 Chesapeake Bay eutrophication model: A report to the US Environmental Protection Agency Chesapeake Bay Program and to the US Army Engineer Baltimore District, *Tech. rep.*, US Army Engineer Research and Development Center, Vicksburg MS.

Cerco, C. F., S.-C. Kim, and M. R. Noel (2013), Management modeling of suspended solids in the Chesapeake Bay, USA, *Estuarine, Coastal and Shelf Science*, *116*, 87–98, doi: https://doi.org/10.1016/j.ecss.2012.07.009.

Da, F., M. A. M. Friedrichs, and P. St-Laurent (2018), Impacts of atmospheric nitrogen deposition and coastal nitrogen fluxes on oxygen concentrations in Chesapeake Bay, *J. Geophys. Res.: Oceans*, *123*, 5004–5025, doi:https://doi.org/10.1029/2018jc014009.

Feng, Y., M. A. M. Friedrichs, J. Wilkin, H. Tian, Q. Yang, E. E. Hofmann, J. D. Wiggert, and R. R. Hood (2015), Chesapeake bay nitrogen fluxes derived from a land-estuarine ocean biogeochemical modeling system: Model description, evaluation, and nitrogen budgets, *J. Geophys. Res. Biogeosciences*, *120*(8), 1666–1695, doi:https://doi.org/10.1002/2015JG002931.

Hagy, J. D., W. R. Boyton, C. W. Keefe, and K. V. Wood (2004), Hypoxia in Chesapeake Bay, 1950–2001: Long-term change in relation to nutrient loading and river low, *Estuaries*, *27*(4), 634–658.

Hong, B., and J. Shen (2012), Responses of estuarine salinity and transport processes to potential future sea-level rise in the Chesapeake Bay, *Estuarine, Coastal and Shelf Science*, *104-105*, 33–45, doi: https://doi.org/10.1016/j.ecss.2012.03.014.

Irby, I. D., M. A. M. Friedrichs, F. Da, and K. E. Hinson (2018), The competing impacts of climate change and nutrient reductions on dissolved oxygen in Chesapeake Bay, *Biogeosciences*, *15*, 2649–2668, doi: https://doi.org/10.5194/bg-15-2649-2018.

Li, M., Y. J. Lee, J. M. Testa, Y. Li, W. Ni, W. M. Kemp, and D. M. Di Toro (2016), What drives interannual variability of hypoxia in Chesapeake Bay: Climate forcing versus nutrient loading?, *Geophysical Research Letters*, *43*, 2127–2134, doi:https://doi.org/10.1002/2015GL067334.

Li, Y., M. Li, and W. M. Kemp (2015), A budget analysis of bottom-water dissolved oxygen in Chesapeake Bay, *Estuaries and Coasts*, *38*, 2132–2148, doi:https://doi.org/10.1007/s12237-014-9928-9.

Lomas, M. W., P. M. Gilbert, F. K. Shiah, and E. M. Smith (2002), Microbial processes and temperature in Chesapeake Bay: Current relationships and potential impacts of regional warming, *Global Change Biology*, *8*(1), 51–70, doi:https://doi.org/10.1046/j.1365-2486.2002.00454.x.

Ni, W., M. Li, A. Ross, and R. G. Najjar (2017), Downscaling climate projections for Chesapeake Bay hypoxia in the mid-21st century, *presentation at the 24th biennial CERF conference, Nov. 5–9, 2017, Providence RI*.

Shchepetkin, A. F., and J. C. McWilliams (2005), The Regional Oceanic Modeling System (ROMS): A split-explicit, free-surface, topography-following-coordinate oceanic model, *Ocean Model.*, *9*, 347–404, doi:https://doi.org/10.1016/j.ocemod.2004.08.002.

Shenk, G. W., and L. C. Linker (2013), Development and application of the 2010 Chesapeake Bay watershed total maximum daily load model, *Journal of the American Water Resources Association*, *49*(5), 1042–1056, doi:https://doi.org/10.1111/jawr.12109.

Testa, J. M., Y. Li, Y. J. Lee, M. Li, D. C. Brady, D. M. Di Toro, W. M. Kemp, and J. J. Fitzpatrick (2014), Quantifying the effects of nutrient loading on dissolved O_2 cycling and hypoxia in Chesapeake Bay using a coupled hydrodynamic-biogeochemical model, *J. Mar. Syst.*, *139*, 139–158, doi: https://doi.org/10.1016/j.jmarsys.2014.05.018.

Wang, P., L. Linker, H. W. ang G. Bhatt, G. Yactayo, K. Hinson, and R. Tian (2017), Assessing water quality of the Chesapeake Bay by the impact of sea level rise and warming, in *Third International Conference on Water Resource and Environment (WRE2017)*, IOP Conf. Series: Earth and Environmental Science 82, 012001, pp. 1–25, Institute of Physics (IOP) Publishing, doi:https://doi.org/10.1088/1755-1315/82/1/012001.

Ye, F., Y. J. Zhang, H. V. Wang, M. A. M. Friedrichs, I. D. Irby, E. Alteljevich, A. Valle-Levinson, Z. Wang, H. Huang, J. Shen, and J. Du (2018), A 3D unstructured-grid model for Chesapeake Bay: Importance of bathymetry, *Ocean Modelling*, *127*, 16–39, doi:https://doi.org/10.1016/j.ocemod.2018.05.002.